Applied Catalysis B: Environmental 297 (2021) 120445

Contents lists available at ScienceDirect

Applied Catalysis B: Environmental

journal homepage: www.elsevier.com/locate/apcatb

Effect of reaction conditions on the deactivation by coke of a $NiAl_2O_4$ spinel derived catalyst in the steam reforming of bio-oil

Naiara García-Gómez, José Valecillos *, Aingeru Remiro, Beatriz Valle, Javier Bilbao, Ana G. Gayubo

Department of Chemical Engineering, University of the Basque Country (UPV/EHU), P.O. Box 644, Bilbao, 48080 Spain

ARTICLE INFO

Keywords:
Bio-oil steam reforming
Hydrogen
$NiAl_2O_4$ spinel
Deactivation
Coke deposition

ABSTRACT

The steam reforming of bio-oil is a promising and economically feasible technology for the sustainable H_2 production, yet with the main challenge of designing highly active and stable catalysts. This work aimed to study the deactivation mechanism of a $NiAl_2O_4$ spinel derived catalyst, the role of Ni and alumina sites in this mechanism and the appropriate reaction conditions to attenuate deactivation. The reaction tests were carried out in a fluidized bed reactor with prior separation of the pyrolytic lignin. The fresh or used catalysts were characterized using X-ray diffraction, temperature-programmed oxidation, X-ray photoelectron spectroscopy, scanning electron microscopy combined with energy dispersive X-ray spectroscopy, and Raman spectroscopy. For steam/carbon ratios > 3.0, space time above 0.075 h and temperature between 600−700 °C, high initial hydrogen yield is obtained (in the 85–90 % range) with CO yield near 20 %, CH_4 yield below 5 % and negligible initial yield of hydrocarbons. The catalyst is more stable at 600 °C, with coke formation preferentially located on Ni sites inside the catalyst particle. Increasing the temperature favors the coke development and consequent deposition on the alumina support, leading to a rapid catalyst deactivation because the limited availability of Ni and alumina sites. These results contribute to understand the phenomenon of catalyst deactivation in the steam reforming of bio-oil and set appropriate reaction conditions to mitigate this problem with a $NiAl_2O_4$ spinel derived catalyst.

1. Introduction

The necessary energy transition towards a sustainable model implies the progressive depletion of fossil fuels and their substitution with environmentally friendly energy vectors. Among several alternatives, hydrogen is a promising energy vector because it is a clean fuel and it has the maximum energy capacity [1]. The current industrial routes for the hydrogen production include thermochemical processes of fossil resources (96 % of the production), and water electrolysis and as a byproduct of other processes. The most common thermochemical process is the endothermic steam reforming (SR) of methane or liquid hydrocarbons of fossil origin [2,3]. However, the use of these raw materials makes the hydrogen production through SR unsustainable, and the challenge is to develop processes based on renewable raw materials, such as biomass. On this regards, most of the efforts focus on the SR of biomass derivatives, particularly that of bio-oil (SRB) [4–6]. Bio-oil is the liquid product from the fast pyrolysis of lignocellulosic biomass [7] or sewage sludge [8] composed of an oxygenate mixture (carboxylic acids, alcohols, aldehydes, ketones, esters, furfurals, phenolic and sugar-like compounds). The interest of the SRB for the H_2 production is motivated by different circumstances [9,10]: (i) the costly dehydration process is avoided; (ii) the existence of well-developed technologies of fast pyrolysis for bio-oil production from lignocellulosic biomass; (iii) the higher volumetric energy density and easier transportation and storage of bio-oil compared to biomass, and; (iv) the perspectives of the strategy of combining the delocalized pyrolysis of biomass with the reforming of bio-oil centralized in a plant with the equipment required by the catalytic processes.

The main reactions in the SRB are the SR of bio-oil oxygenates (Eq. (1)) and water gas shift (WGS) (Eq. (2)), and the combination of these two reactions corresponds to the stoichiometry of Eq. (3). Nevertheless, many other secondary reactions take place simultaneously, that contribute to the decrease in the hydrogen yield and the formation of carbonaceous deposits (coke) that deactivate the catalyst. These

* Corresponding author.
E-mail address: jose.valecillos@ehu.eus (J. Valecillos).

https://doi.org/10.1016/j.apcatb.2021.120445
Received 10 March 2021; Received in revised form 8 June 2021; Accepted 9 June 2021
Available online 11 June 2021

secondary reactions include: the decomposition of oxygenates (Eq. (4)) that yields methane, carbon oxides, light hydrocarbons and coke; the SR of methane (Eq. (5)) and light hydrocarbons (also formed as byproducts of dehydration/cracking reactions of oxygenates) (Eq. (6)); the Boudouard reaction (Eq. (7)) that yields coke, and; other decomposition reactions that lead to the equilibrium formation-gasification of coke (Eqs. (8)–(10)).

Steam reforming of oxygenates:

$$C_nH_mO_k + (n - k)H_2O \rightarrow nCO + (n + m/2 - k)H_2 \quad (1)$$

Water gas shift (WGS) reaction:

$$nCO + nH_2O \leftrightarrow nCO_2 + nH_2 \quad (2)$$

Global SR of bio-oil (SRB) reaction:

$$C_nH_mO_k + (2n - k)H_2O \rightarrow nCO_2 + (2n + m/2 - k)H_2 \quad (3)$$

Decomposition/dehydration/cracking of oxygenates:

$$C_nH_mO_k \rightarrow C_xH_yO_z + C_rH_s + CH_4 + H_2O + CO + CO_2 + H_2 + C(coke) \quad (4)$$

Steam reforming of methane and light hydrocarbons:

$$CH_4 + H_2O \leftrightarrow CO + 3H_2 \quad (5)$$

$$C_rH_s + rH_2O \rightarrow rCO + (r + s/2)H_2 \quad (6)$$

Boudouard reaction:

$$2CO \leftrightarrow CO_2 + C(Coke) \quad (7)$$

Coke formation/gasification:

$$CH_4 \leftrightarrow 2H_2 + C(coke) \quad (8)$$

$$C_rH_s \rightarrow (s/2)H_2 + rC(coke) \quad (9)$$

$$C(coke) + H_2O \rightarrow CO + H_2 \quad (10)$$

The challenges are maximizing the hydrogen yield and preventing coke formation that leads to catalyst deactivation, which can be controlled with an appropriate catalyst design and the optimization of the reaction conditions. The catalyst design for the SRB points out to the use of natural materials (of low cost because of their availability, such as dolomite, olivine, limestone), supported non-noble metals (Ni, Co, Cu, Fe) and supported noble metals (Pd, Pt, Ru, Rh) [11]. Those based on Ni receive great attention for the SRB [11,12], steam reforming of volatiles from biomass fast pyrolysis [13] and tar (byproduct from biomass gasification) [14], because of their outstanding relationship between costs and performance. In Ni supported catalysts, both Ni and support sites have specific functions for steam reforming reactions. The most active Ni sites are reduced Ni crystals that are responsible for the adsorption and C—C bond scission of oxygenates [12,15]. Likewise, Ni sites are able to adsorb and dissociate water that is an elemental step in steam reforming reactions [16].

The main function of the support is to disperse the Ni sites to provide larger specific surface area of the active sites. Additionally, the support sites provide synergetic functions according to their nature, being the water adsorption and dissociation a common feature for many materials [12]. The conventional catalyst support is γ-Al_2O_3 because of its high capacity to disperse Ni crystals [17]. However, the γ-Al_2O_3 acid sites promote the formation of coke precursors giving rise to a high coke formation that can be attenuated with the passivation of the acid sites using CeO_2 or La_2O_3 [18]. The presence of these promoters improves the dispersion and prevent the sintering of Ni sites, and enhance the water adsorption and dissociation. Additionally, the CeO_2 incorporation as a promoter provides oxygen vacancies and increases the activity of coke gasification [19].

The regeneration capacity is an essential requirement of the Ni catalysts to be used in SRB because of the rapid deactivation by coke [20–22]. In this regard, some recent advances in catalyst design can be highlighted. Kumar and Sinha [23] have developed a Ni/γ-Al_2O_3-La_2O_3-CeO_2 catalyst using metal organic frameworks (MOF) that is active for the SR of acetic acid with an remarkable stability. This catalyst almost recovers its complete activity upon the coke combustion with oxygen at 500 °C [24]. The catalyst derived from $NiAl_2O_4$ spinel is highly active for the SRB, and shows an appropriate regeneration capacity upon the coke combustion, which makes it appropriate for reaction-regeneration cycles [9,25–27]. The actual catalyst results from the reduction of the $NiAl_2O_4$ spinel structure that leads to well-dispersed Ni crystals supported on Al_2O_3 giving rise to a high activity [28]. The advantage of preparing Ni supported catalysts from $NiAl_2O_4$ spinel rely on the incorporation of high Ni loadings with high dispersion in the catalyst particle, which is an advantage to reduce coke formation [29].

The reaction conditions (temperature, steam/carbon (S/C) ratio and space time) significantly affect the catalyst performance because of their impact on the extent of the reactions involved in the SRB (Eqs. (1), (2) and (4)–(10)) that are governed by thermodynamic equilibria [11, 30–36]. The effect of temperature is complex given the endothermic nature of the SR reactions (Eqs. (1), (5) and (6)) and the moderate exothermic nature of the WGS reaction (Eq. (2)). Thus, the increase in the reaction temperature favors the extent of the SR reactions and disfavors the WGS reaction. Likewise, the increase in the reaction temperature favors the undesired decomposition/cracking of oxygenates (Eq. (4)) and disfavors the coke formation through the Boudouard reaction (Eq. (7)), whereas the coke gasification reactions (Eq. (10) and reverse of Eqs. (7) and (8)) are also favored [20–22,35,37].

Another important reaction condition is the steam/carbon (S/C) ratio in the feed since an excess of water above the stoichiometric value favors the SR (Eqs. (1), (5) and (6)) and WGS (Eq. (2)) reactions and also favors the coke gasification reaction (Eq. (10)) at high temperatures [36, 38]. However, the blockage of the catalytic sites by the water molecules may hinder the adsorption of oxygenates causing a decrease in the catalytic activity [39]. Furthermore, it is important to consider that the use of high values of temperature and S/C ratio in the feed may lead to the sintering phenomenon causing irreversible catalyst deactivation [40] and increases the energy requirements of the process [36]. Finally, the increase in the space time (ratio between the catalyst weight and reactant flowrate) increases the availability of catalytic sites and consequently favors the extent of the reaction steps with the aim of approaching to the thermodynamic equilibrium, boosting the conversion of oxygenates and hydrogen yield [33,41,42].

As aforementioned, catalyst deactivation by coke deposition is one of the most relevant challenges in the SRB and understanding this phenomenon is paramount for an appropriate catalyst and process design. The catalyst deactivation by coke in the SRB depends on the catalyst characteristics, oxygenate composition and reaction conditions (particularly on the reaction temperature), which affect the coke nature and location on the catalyst with different impacts on catalyst deactivation [20,43]. Some research efforts made to understand this phenomenon reflect the particularities of these variables. The coke deposits on a Ni/La_2O_3-αAl_2O_3 catalyst after the SRB at 550 °C have been found to have an amorphous and encapsulating nature leading to a rapid catalyst deactivation, whereas they have a filamentous nature at 700 °C with a mildly effect on catalyst deactivation [22,44]. Indeed, the coke deposits on a NiCaAl catalyst after the SRB at 800 °C are mostly constituted of filaments (carbon nanotubes) [45]. The formation of filamentous coke is more reliably seen on a Ni/αAl_2O_3 catalyst after the SR of several bio-oil model compounds at 700 °C [46]. Other reaction conditions, such as the S/C ratio in the feed and space time, would have a less severe effect on the nature of coke deposits, with a major impact on their amount and formation rate [20].

In this work, we have investigated the mechanism of deactivation by coke of a $NiAl_2O_4$ spinel derived catalyst in the SRB. The selection of this catalyst is based on its regeneration capacity that makes it a promising alternative for the use at a larger scale in reaction-regeneration cycles.

The regeneration based on the coke combustion and calcination at high temperature (850 °C) re-oxidizes the Ni crystals, and NiO diffuses into the Al_2O_3 lattice to form the $NiAl_2O_4$ spinel structure. The prior reduction of the $NiAl_2O_4$ structure in the reactor generates Ni crystals that are well dispersed on the Al_2O_3 support. The cycle can be repeated and the catalyst recovers the activity for the SRB [26]. Our previous works with this $NiAl_2O_4$ spinel derived catalyst were carried out under selected conditions (700 °C and space time near 0.13 (g catalyst) h (g bio-oil)$^{-1}$ [9,26,27]) based on studies of the SRB with other catalysts (a commercial Rh/CeO_2-ZrO_2 [47,48] or supported Ni/La_2O_3-αAl_2O_3 [38,44,49]). We have further extended our research on deepening the insights into the catalyst deactivation by coke at different reaction conditions (600−700 °C; space time, up to 0.25 (g catalyst) h (g bio-oil)$^{-1}$; and steam/carbon molar ratio (S/C), 1.5–6), with the purpose of establishing adequate reaction conditions for mitigating this problem affecting the process feasibility. For this purpose, we selected low space time values to observe relevant deactivation in our experiments. The used catalysts (those recovered after each experiment) were analyzed by several techniques (X-ray diffraction (XRD), temperature-programmed oxidation (TPO), X-ray photoelectron spectroscopy (XPS), scanning electron microscopy combined with energy dispersive X-ray spectroscopy (SEM-EDX), and Raman spectroscopy), to determine the degree of sintering of Ni crystals, and quantity and characteristics of coke deposits. Our results point out to the significant effect of temperature on the coke nature and location on the $NiAl_2O_4$ spinel derived catalyst, and the benefit of carrying out the SRB at 600 °C.

2. Experimental

2.1. Catalyst preparation and characterization

The $NiAl_2O_4$ spinel structure was synthetized using the co-precipitation method [27,50]. The synthesis procedure consisted of mixing hexa-hydrated nickel nitrate ($Ni(NO_3)_2{\cdot}6H_2O$, Panreac, 99 %) and nona-hydrated alumina nitrate ($Al(NO_3)_3{\cdot}9H_2O$, Panreac, 98 %) in an aqueous solution and adding a 0.6 M solution of ammonium hydroxide (NH_4OH, Fluka, 5 M) as the precipitating agent dropwise until reaching a pH of 8. Afterwards, the precipitate was recovered using filtration and washed with distilled water to remove the remaining ammonium ions. The recovered precipitate was dried for 12 h, calcined at 850 °C for 4 h with a heating ramp of 10 °C min^{-1}, and crushed and sieved to obtain particle sizes in the range of 0.15−0.25 mm. These particles are assumed to have the stoichiometric formula of $NiAl_2O_4$, corresponding to 33 wt% of Ni.

The $NiAl_2O_4$ spinel structure was characterized using temperature-programmed reduction (TPR), XRD and nitrogen physisorption. The TPR analysis was carried out in a Micromeritics AutoChem II 2920 apparatus and the experimental procedure consisted of exposing the sample to a flow of hydrogen (10 mol%) in argon and heating from 50 °C up to 950 °C at 5 °C min^{-1}. The TPR profile (Fig. 1a) shows that the H_2 uptake takes place between 400 and 900 °C, indicating the progressive reduction of Ni species with a maximum at 760 °C, which is a typical reduction temperature for the Ni species attached to the spinel structure [25,51].

The XRD analysis of the reduced catalyst was carried out in a Bruker D8 Advance diffractometer with a CuKα1 radiation. The device is equipped with a Germanium primary monochromator, Bragg-Brentano geometry and with a CuKα1 wavelength of 1.5406 Å, corresponding to an X-ray tube with Cu anticathode. A Sol-X dispersive energy detector was employed, with a window optimized for CuKα1 for limiting the fluorescence radiation. Data collection was carried out continuously, from 10° to 80° with step of 0.04° in 2θ and measurement time of 103 min. The XRD patterns (Fig. 1b) confirm that synthetized $NiAl_2O_4$ spinel has the expected cubic close-packed structure, with intense peaks at 2θ = 37.2, 45.2 and 65.7° [50,51]. Likewise, upon reduction of the $NiAl_2O_4$ structure, the XRD pattern indicates a complete change in the structure

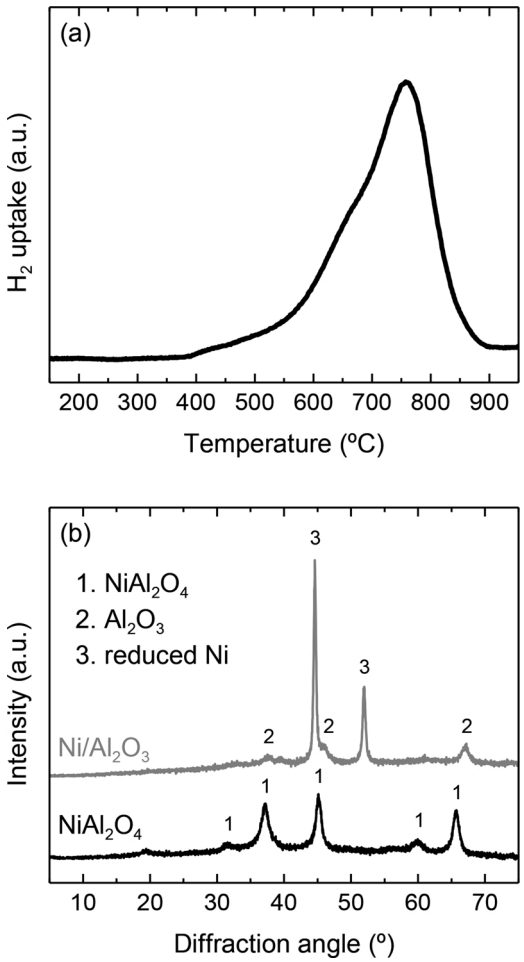

Fig. 1. Characterization of synthetized $NiAl_2O_4$ spinel and derived catalyst: TPR profile (a); XRD patterns (b).

resulting in intense peaks at 2θ = 44.6 and 52.0° corresponding to reduced Ni crystals and at 2θ = 37.5, 46.0 and 67.1° corresponding to Al_2O_3 phases [25]. The Ni crystal size was calculated using the Scherrer equation and the deconvolution parameters of the peak at 2θ = 52.0°, giving an average value of 13 nm.

The derived catalyst morphology was studied using transmission electron microscopy in a Philips SuperTwin CM200 microscope. The TEM image (Fig. S1 in the Supplementary Information) shows that the catalyst is composed of Ni crystals with an almost uniform size and supported on an Al_2O_3 phase. The crystal size distribution determined using the TEM image gives an average value of 12.5 nm, being similar to that determined using the Scherrer equation in agreement with a previous work [26].

The N_2 physisorption was carried out in a Micromeritics ASAP 2010 apparatus and the experimental procedure consisted of outgassing the sample at 150 °C and 10^{-3} mmHg for 8 h followed by the adsorption and desorption of nitrogen at 77 K in order to obtain isotherm data to calculate the specific surface area and volume with the BET method. The textural properties of synthetized $NiAl_2O_4$ spinel and derived catalyst are shown in Table 1. The specific surface area for synthetized $NiAl_2O_4$

Table 1
Textural properties of $NiAl_2O_4$ spinel and derived catalyst.

Sample	S_{BET} (m^2 g^{-1})	V_{pore} (cm^3 g^{-1})	Pore size (nm)
$NiAl_2O_4$ spinel	94	0.217	7.94
Catalyst	68	0.228	12.5

S_{BET} = specific surface area determined with BET method. V_{pore} = pore volume.

spinel is 94 $m^2\ g^{-1}$, whereas is slightly lower for the derived catalyst (68 $m^2\ g^{-1}$), which is comparable to that of a Ni/Al_2O_3 catalyst with a high Ni loading [52]. Likewise, the average pore diameter also increases for the derived catalyst, being larger than that for conventional Ni/Al_2O_3 catalysts or even for Al_2O_3 phases.

Thus, the afore mentioned analysis, give evidence that the $NiAl_2O_4$ spinel structure is completely converted into an Al_2O_3 supported Ni catalyst upon reduction at 850 °C with an isothermal period of 4 h to assure the reduction of all Ni species in $NiAl_2O_4$ spinel prior to each experiment. Furthermore, the relative high surface area and mean pore size of the resulting catalyst would allow the diffusion of reactants through the catalyst particle.

The used catalysts (those used in each reaction test) were analyzed using XRD, TPO, XPS, SEM with a secondary electron detector or backscatter electron detector (BSD-SEM) alone or combined with energy-dispersive X-ray spectroscopy (EDS), and Raman spectroscopy. The TPO analyses were carried out in a Thermo Scientific TGA Q5000TA IR thermobalance coupled in line with a Thermostar Balzers Instrument mass spectrometer for monitoring the CO_2 signal (m/z = 44). The TPO profile was quantified using the mass spectrometric data of the CO_2 signal because the oxidation of Ni crystals during combustion might mask the thermogravimetric signal. The procedure consisted of stabilizing the sample at 50 °C, followed by heating at 5 °C min^{-1} up to 800 °C under an airflow at 50 $cm^3\ min^{-1}$. The XPS spectra were carried out in a SPECS (Berlin, Germany) system equipped with a Phoibos 150 1D-DLD analyzer, Al Kα monochromatic radiation (1486.6 eV), an X-ray exciting source, and a hemispherical electron analyzer. The binding energy of the C 1s carbon was set at 284.6 eV to correct the material charging, and the analysis was carried out using an electron take off angle of 90°. The SEM images were obtained in a JEOL JSM-7000F microscope with a tungsten filament (resolution 3.5 nm) equipped with an Oxford Pentafet EDS analyzer (resolution 133 eV) operating at 20 kV under vacuum at 9.65×10^{-5} bar and an intensity of 1.85×10^{-10} A. Additionally, high resolution SEM images were obtained in Hitachi S-4800 N field emission gun scanning electron microscope (FEG-SEM) using an accelerating voltage of 5 kV. The Raman spectra were carried out in a Renishaw InVia confocal microscope using an excitation wavelength of 514 nm, taking a spectrum in several areas of the sample for assuring reproducibility.

2.2. Bio-oil

Bio-oil was supplied by BTG Bioliquids BV (The Netherlands) and was obtained through flash pyrolysis of pine sawdust in an industrial plant with a conical rotary reactor for a capacity of 5 t h^{-1}. The bio-oil density is 1.105 g ml^{-1}. The water content of bio-oil was determined using Karl-Fischer titration (KF-Titrino Plus 870) giving 26 wt%. The elemental analysis was determined using a Leco CHN-932 analyzer (water-free basis), resulting in an empiric formula of $C_{4.6}H_{6.2}O_{2.4}$. The chemical composition was determined using a Shimadzu QP2010S gas chromatography/mass spectrometer (GC/MS) provided with a BPX-5 column (50 m × 0.22 mm x0.25 μm) and mass selective detector. Identification of compounds was accomplished by matching the mass spectra with NIST 147 and NIST 27 data libraries. The main compounds are listed in Table 2.

Table 2
Semi-quantitative GC–MS composition (% peak area) of raw bio-oil.

Components	Composition (%)
ACIDS	10.0
Acetic acid	8.0
KETONES	20.4
Linear	15.0
Acetone	5.6
Acetol	5.6
Cyclic	5.4
ESTERS	3.7
FURANONES	6.9
ALCOHOLS	4.1
ALDEHYDES	5.0
ETHERS	1.9
SACCHARIDES	21.4
Levoglucosan	14.4
PHENOLS	26.7
Alkyl-phenols	2.8
Guaiacols	12.4
Catechols	6.4
Syringols	0.1
Other	4.8

2.3. Reaction tests

The SRB experiments were carried out in a continuous two-units reaction equipment (MicroActivity Reference from PID Eng&Tech) shown in Fig. S2 (Supplementary Information). The first unit is a U-shaped steel tube (inner diameter = 0.75 in.) for the vaporization of bio-oil and the controlled deposition of pyrolytic lignin (PL) formed through repolymerization of some oxygenates (mainly phenolic compounds) during the vaporization of bio-oil [53]. In this way, the subsequent deactivation of the SR catalyst is attenuated, although there is a moderate decrease in the flowrate of oxygenates that enters the reforming reactor (Unit 2). The temperature in this first unit was 500 °C, which appropriately balances the amount of oxygenates exiting the unit and the stability of the catalyst in the subsequent reforming reactor [40]. This second unit is a fluidized-bed reactor for reforming the effluent stream of the first unit. The reactor (of stainless steel, with 22 mm of internal diameter and total length of 460 mm) is located inside a furnace with a steel casing, covered with refractory material and with an electrical resistance inside. The reactor-furnace assembly is located in a hot box at 300 °C, to avoid condensation of the inlet streams to the reactor, as well as the outlet stream before being sent for on-line analysis. In order to improve the fluidodynamics of catalytic bed, the catalyst ($NiAl_2O_4$ spinel with a particle size of 0.15−0.25 mm) is mixed with a solid inert material (silicon carbide with a particle size of 0.037 mm), with an inert/catalyst mass ratio above 8.

The feed to the reaction equipment consists of a mixture of (1) raw-bio oil pumped at 0.08 mL min^{-1} with a Harvard Apparatus 22 injection pump, (2) water pumped at the required flowrate according to the desired S/C ratio with a 307 Gilson pump, and (3) nitrogen at balanced flowrates according to the required amount of water, so that the total feed flowrate remains in the 800−1000 ml min^{-1} range (in reforming reaction conditions). A small portion of the effluent stream of the second unit (fluidized-bed reactor) is diluted in an He stream and sent continuously through a thermally insulated line (at 150 °C) to a micro gas chromatograph (MicroGC 490 Agilent) for the on-line analysis of its composition. The MicroGC is provided with four columns: molecular sieve MS5 (for hydrogen, oxygen, nitrogen, methane and carbon monoxide), Plot Q (for carbon dioxide, water and C_2-C_4 hydrocarbons), CPSIL (for C_5-C_{11} hydrocarbons, not detected in this work), and Stabilwax (for oxygenates).

Prior to each SRB experiment, the catalyst was reduced in situ under a hydrogen (10 mol%)-nitrogen flow at 850 °C for 4 h. These conditions are appropriate for the complete reduction of the Ni species in the $NiAl_2O_4$ structure leading to obtain well-dispersed Ni crystals on Al_2O_3. The SRB experiments were carried out in individual sets of variable reaction temperature (600, 650 and 700 °C), variable space time by changing the catalyst load and variable steam/carbon (S/C) molar ratio in the feed (1.5, 3.0, 4.3 and 6.0) by balancing the water and nitrogen flowrates, keeping the rest of the experimental conditions constant in each set of experiments. The space time (W/F_0) is defined as the ratio between the catalyst weight (W) and the flowrate of oxygenates in the main feed stream (F_0), with values between 0.075 and 0.25 (g catalyst) h (g oxygenates)$^{-1}$ (hereafter the units for the space time will be

simplified to h). These reaction conditions were selected based on our previous experience in the SRB with other catalysts [38,44,48,49]. After each experiment, the used catalyst was recovered and kept for analyses as described in the Section 2.1.

The main detected products in the effluent stream of the second unit were hydrogen (H_2), carbon monoxide (CO), carbon dioxide (CO_2), methane (CH_4) and C_2-C_4 hydrocarbons (HC). By using the experimental data, the conversion of oxygenates in bio-oil (X) was calculated as:

$$X = \frac{F_{oxygenates,in} - F_{oxygenates,out}}{F_{oxygenates,in}} \quad (11)$$

Where $F_{oxygenates}$ is the carbon-based molar flowrate of oxygenates in the bio-oil in the feed (in) or in the effluent (out) streams of the second unit. The $F_{oxygenates,in}$ was calculated by subtracting the amount of deposited LP in the first unit from the oxygenates flowrate of the main feed stream (F_0). The $F_{oxygenates,in} - F_{oxygenates,out}$ was calculated from the sum of carbon-based molar flowrates of gaseous carbon products (CO, CO_2, CH_4 and HCs) in the effluent stream. The H_2 yield (Y_{H2}) was calculated as:

$$Y_{H2} = \frac{F_{H2,out}}{F_{H2,stoichiometry}} \quad (12)$$

Where $F_{H2,out}$ is the hydrogen flowrate in the effluent (out) stream of the second unit and $F_{H2,stoichiometry}$ is the stoichiometric hydrogen flowrate that would be formed according to the overall SR reaction of oxygenates (Eq. (3)). The yield of the carbon products (Y_i, where i = CO, CO_2, CH_4 and HC) was calculated as:

$$Y_i = \frac{F_{i,out}}{F_{oxygenates,in}} \quad (13)$$

Where $F_{i,out}$ is the carbon-based molar flowrate of the i product in the effluent (out) stream of the second unit.

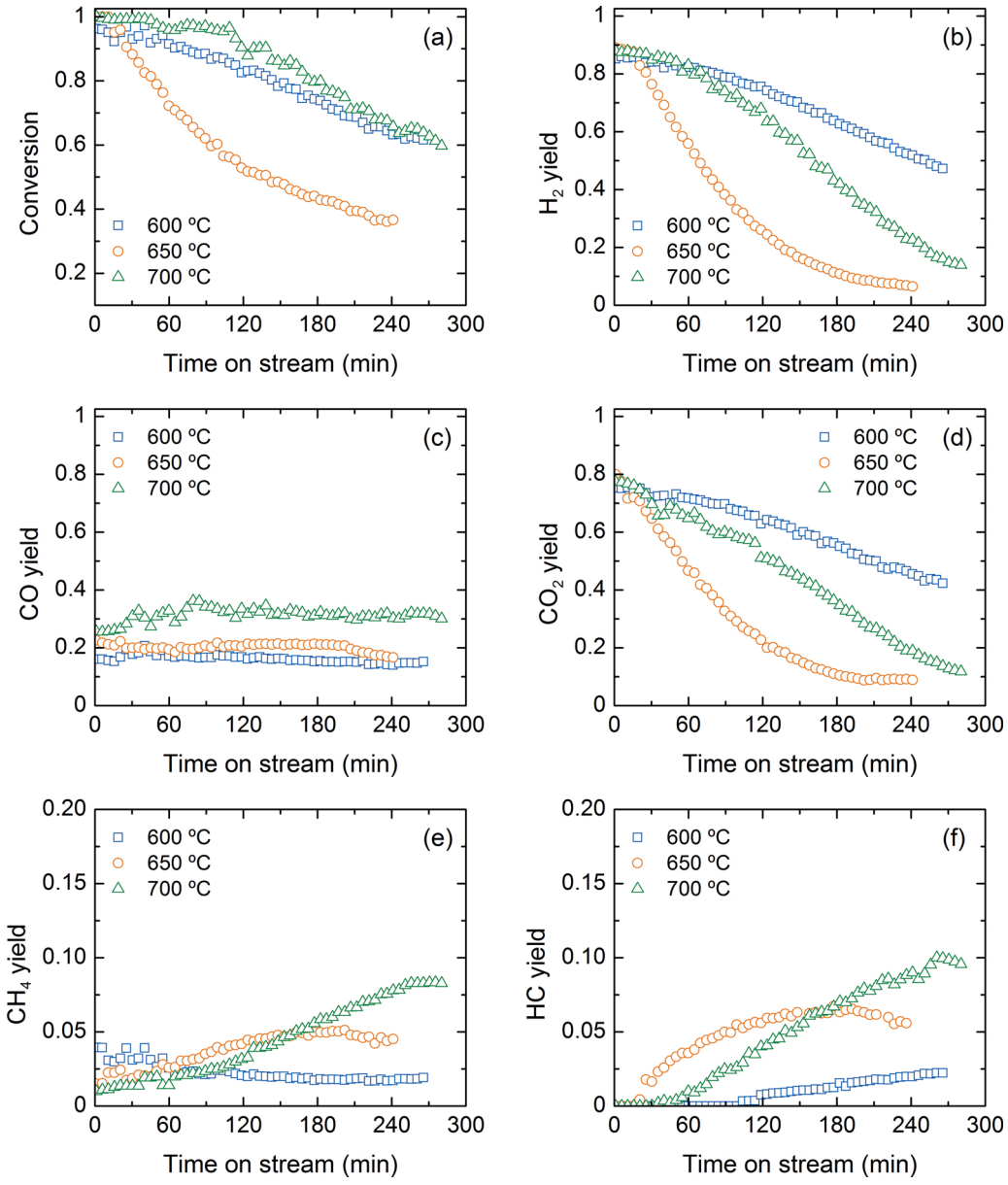

Fig. 2. Effect of reaction temperature on the evolution with time on stream of the conversion of oxygenates (a) and yield of H_2 (b), CO (c), CO_2 (d), CH_4 (e) and hydrocarbons (HC) (f). Reaction conditions: space time, 0.15 h; S/C ratio, 3.0.

3. Results

3.1. Effect of reaction conditions

This section presents the results for the effect of reaction conditions on the performance of the $NiAl_2O_4$ spinel derived catalyst in the SR of bio-oil (SRB). Specifically, the effect of temperature, space time and steam/carbon (S/C) molar ratio in the feed on the evolution with time on stream of the conversion and yield of products is individually analyzed in the following subsections.

3.1.1. Temperature

Fig. 2 shows the effect of reaction temperature on the evolution with time on stream of the conversion (Fig. 2a) and yield of products (Figs. 2b–f) for a space time of 0.15 h and S/C ratio of 3. This low space time value enables to obtain experimental data under a kinetic regime to clearly analyze the effect on the catalyst deactivation. As seen in Fig. 2, the conversion at zero time on stream increases with increasing temperature values, reaching complete conversion at 650 °C and 700 °C. This high conversion at zero time on stream evidences a high activity of the fresh catalyst, which is consistent with the availability of Ni sites and the structural properties, thus allowing the diffusion of reactants through the catalytic sites (properties described in Section 2.1). Additionally, Figs. S3 and S4 in the Supplementary Information show the effect of reaction temperature for a space time of 0.075 h and S/C = 1.5 and 0.15 h and S/C = 1.5, respectively. At these conditions (lower space time and/or S/C ratio values than those of Fig. 2), the deactivation is severer.

The initial H_2 and CO_2 yield (Figs. 2b and d, respectively) reaches a maximum at 650 °C, whereas the values are slightly higher at 700 °C than at 600 °C. The maxima in the H_2 and CO_2 yield as a function of the reaction temperature is an expected result for the SRB [11], and it occurs by the thermodynamically favored reverse WGS reaction (inverse of Eq. (2)) at high temperature values [54] (in this case above 650 °C), which reduces the H_2 and CO_2 formation. The maxima in the H_2 and CO_2 yield is also observed at other reaction conditions (Fig. S4). On the other hand, the initial CH_4 yield (Fig. 2e) decreases with increasing temperature values, confirming that the SR of methane is favored (Eq. (5)) [55]. The initial yield of HC is insignificant at almost all reaction conditions (Figs. 2f, S3f and S4f) except for the lower temperature and space time values), which evidences the high capacity of the $NiAl_2O_4$ spinel derived catalyst for reforming these byproducts (Eq. (6)) formed from the cracking/dehydration/decomposition of oxygenates (Eq. (4)).

The decrease in the conversion with increasing time on stream at all the temperature values (Fig. 2a) evidences that the catalyst undergoes deactivation, with the order in the deactivation rate being 650 °C >> 700 °C > 600 °C. This order is also observed at other reaction conditions (Figs. S3 and S4). At all the temperatures, the catalyst deactivation causes a decrease in the H_2 and CO_2 yield (Figs. 2b and d, respectively) and an increase in the HC yield (Fig. 2f), which is more rapid at 650 °C according to the more rapid decrease in the conversion. This indicates that the catalyst is deactivated to so extent for the SR reactions (of both oxygenates and hydrocarbons) and WGS reaction. This deactivation is practically complete at 650 °C and 700 °C after 4 and 4.5 h on stream, respectively, whereas at 600 °C the catalyst remains partially active after 4.5 h on stream (indicated by the relative high H_2 and CO_2 yield). Although the main objective is the production of H_2, it can be observed that with the catalyst deactivated after 4.5 h on stream a higher yield of useful syngas (H_2 and CO) is obtained at 700 °C than at 600 °C. This result is explained because the extent of the reverse WGS reaction (reverse of Eq. (2)) and thermal decomposition of oxygenates (Eq. (4)) are favored at high temperature, contributing to the formation of H_2, CO and CH_4. The evolution with time on stream of the CO and CH_4 yield significantly varies depending on the reaction temperature. The CO yield (Fig. 2c) remains almost constant at 600 and 650 °C, and slightly increase at 700 °C, whereas the CH_4 yield (Fig. 2e) decreases at 600 °C, and increases at 650 and 700 °C. This is an expected result for intermediate products in the overall reaction scheme, and it is a consequence of the different impact of the reaction conditions on the reaction steps and on the formation and disappearance of coke, and consequently on the catalyst deactivation [42].

Thus, at high temperature values (when the methane SR reaction (Eq. (5)) is highly promoted over methanation reaction (reverse of Eq. (5)), CH_4 is mainly a primary product in the reaction scheme, and consequently, its yield increases with increasing time on stream when the catalyst is deactivated for the methane SR reaction. Nevertheless, at 600 °C (when the methanation reaction is favored over the methane reforming reaction), CH_4 is mainly a final product in the overall reaction scheme, and consequently, its yield decreases continuously with time on stream as the catalyst undergoes deactivation for the methanation reaction. The constant values of the CO yield with time on stream evidence its role as an intermediate product in the reaction scheme, and a similar impact of catalyst deactivation on its formation reactions (by cracking/decomposition and reforming of oxygenates, Eqs. (4) and (1), respectively) and on the disappearance reaction by the WGS and methanation reactions (Eq. (2) and reverse of Eq. (5), respectively). Nevertheless, for low S/C ratio values (Figs. S3 and S4), when the SR or WGS reactions are disfavored, the decrease in the CO yield with time on stream could be explained by the deactivation of the catalyzed decomposition/cracking reactions of oxygenates, being more rapid at higher temperature values. It should be noted that as the deactivation of the catalyzed reactions progresses, the yields of products tend to those obtained by thermal routes of decomposition/cracking of oxygenates (Eq. (4)),(values in Table S1, in Supplementary Information). These thermal routes are favored at increasing temperature values. Consequently, for highly deactivated catalysts, the CO, CH_4 and HC yield increases with increasing reaction temperature values [47].

The explanation for the maximum deactivation rate at an intermediate reaction temperature (650 °C) lies in the opposite effect of temperature in the coke formation and gasification reactions. The increase in the reaction temperature favors coke formation through the decomposition/dehydration/cracking of oxygenates (Eq. (4)) and decomposition of methane (Eq. (8)) and hydrocarbons (Eq. (9)), although it disfavors the coke formation through the Boudouard reaction (Eq. (7)), and it also favors the coke gasification (Eq. (10)). Based on our results, we infer that the coke formation reactions prevail at 650 °C.

3.1.2. Space time

The effect of space time on the SRB was assessed by varying the catalyst weight in each experiment while keeping constant the bio-oil flowrate and the rest of operating conditions (temperature and S/C ratio). Fig. 3 shows the effect of space time (0.075, 0.15 or 0.25 h) at 700 °C and S/C ratio in the feed of 3. Additionally, Figs. S5 and S6 show the effect of space time at 600 °C and S/C = 6, and at 650 °C and S/C = 1.5, respectively.

As seen in Fig. 3a, the conversion is complete (around 1) at zero time on stream and the corresponding yield of products (Figs. 3b–f) is similar for the different space time values because of the use of a high reaction temperature value (700 °C). Nevertheless, at low reaction temperature values (600 °C in Fig. S5 or 650 °C in Fig. S6), the initial conversion and product yield are lower and noticeably increase with increasing space time values because of the favored extent of the reactions, particularly that of the SR and WGS reactions [47]. It should be noted that the initial CH_4 yield increases with increasing space time (Fig. 3e). This result evidences the significant contribution to the overall reaction scheme of the catalytic reactions of decomposition/cracking of oxygenates (Eq. (4)) at high temperature, which are slow reactions their rate are accelerated using a higher amount of catalyst. A general conclusion from these results is that the use of this $NiAl_2O_4$ spinel derived catalyst accelerates the SR and WGS reactions favoring the H_2 formation in comparison to the thermal reactions (without using a catalyst) (Table S1), with a good approaching to the thermodynamic equilibrium at high

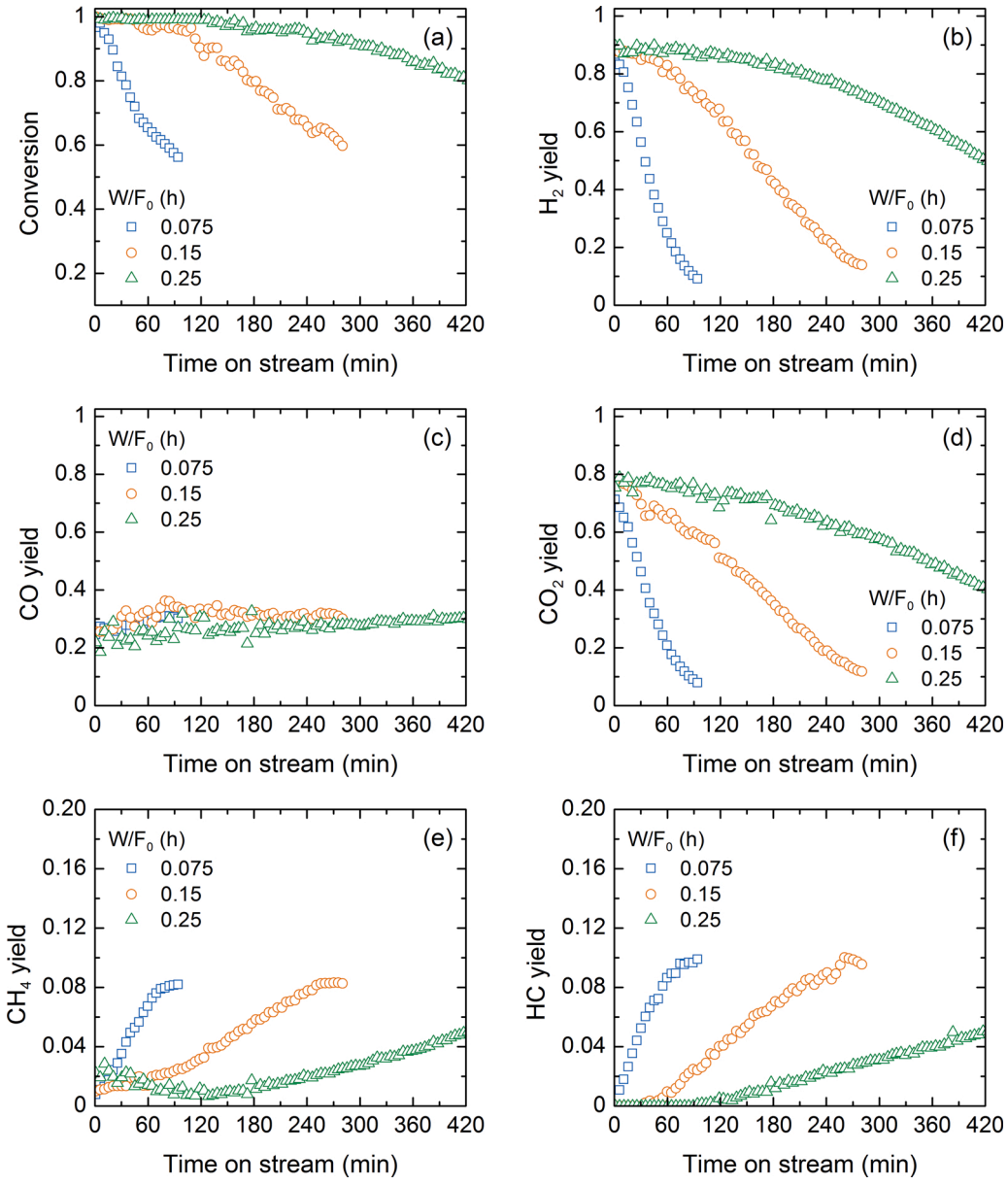

Fig. 3. Effect of space time (W/F_0) on the evolution with time on stream of the conversion of oxygenates (a) and yield of H_2 (b), CO (c), CO_2 (d), CH_4 (e), and hydrocarbons (HC) (f). Reaction conditions: 700 °C; S/C ratio, 3.0.

space time values [36].

The performance of the $NiAl_2O_4$ spinel derived catalyst is comparable with other catalysts at similar conditions (high space time approaching the equilibrium, 700 °C and S/C ratio of around 3). On a Ni/La_2O_3-Al_2O_3 catalyst, Valle et al. [49] obtained complete conversion and a H_2 yield around 90 %. On a Rh/CeO_2-ZrO_2 catalyst, with a higher S/C ratio (6), Remiro et al. [48] obtained complete conversion and a H_2 yield of 95 %. Bali et al. [56] observed different performance for a Ni spinel catalyst without prior reduction, using different bio-oil feeds at lower S/C ratio values and higher temperature values.

On the other hand, Fig. 3 (corresponding to 700 °C and S/C = 3) shows that the deactivation rate (inferred from the decrease in the conversion with increasing time on stream in Fig. 3a) decreases noticeably with increasing space time values. The H_2 and CO_2 yield decreases with time on stream (Figs. 3b and d, respectively) and the HC yield (Fig. 3f) increases, due to the catalyst deactivation for the SR and WGS reactions. These variations in products yields are slower for higher values of space time, in line with the attenuation in the deactivation rate at high space time values observed in Fig. 3a. These trends are similar at 600 °C and S/C = 6 (Fig. S5), and at 650 °C and S/C = 1.5 (Fig. S6). Comparing the results in Figs. 3, S5 and S6, it is observed that the CO and CH_4 yield show different trends with time on stream depending on the reaction temperature and S/C ratio in the feed. Thus, a high enough S/C ratio (Figs. 3 and S5) promotes the WGS reaction, and at these conditions the CO yield remains almost constant with time on stream, due to the similar impact of deactivation on the reactions forming CO (reforming (Eqs. (1), (5) and (6)) and catalytic decomposition/cracking (Eq. (4)) reactions) and on the reaction accounting for its disappearance (WGS reaction (Eq. (2)). Nevertheless, for a low S/C ratio (Fig. S5), the WGS reaction is not promoted, and at these conditions, CO is mainly a final product, whose yield decreases with time on stream when the catalyst is deactiavted for its forming reactions. At 700 °C, the CH_4 yield overall increases with time on stream (Fig. 3e), evidencing that it is mainly a primary product in the reaction, whose yield increases when the catalyst is deactivated for the methane reforming reaction (Eq. (5)) and this increase is slower for high space time values in agreement with

the attenuation of catalyst deactivation. Nevertheless, at the highest space time value the CH_4 yield decreases at the beginning of the run, passes through a minimum and subsequently increases continuously. This peculiar behavior can be explained because the catalytic decomposition/cracking reactions (whose extent is relevant at high space time) are slow reactions that are more rapidly affected by the deactivation of the catalyst than the methane reforming reaction. At 600 °C (Fig. S5), the catalyst remains partially active even for a low space time of 0.15 h. At 700 °C (Fig. 3), the catalyst remains active at the highest space time value (0.25 h), and at 650 °C (Fig. S6), the catalyst undergoes severe deactivation at all the space time values.

3.1.3. Steam/carbon ratio

The effect of steam/carbon (S/C) molar ratio in the feed was assessed by varying the water and nitrogen flowrates while keeping constant the bio-oil flowrate. Fig. 4 shows the evolution with time on stream of the conversion and yield of products at 700 °C and space time of 0.25 h and different S/C ratio values in the feed (1.5, 3.0 and 4.3). As seen, the conversion and the H_2 and CO_2 yield at zero time on stream increase whereas the CO and CH_4 yield decreases with the increase in the S/C ratio in the feed. These trends in the conversion and yield of products with increasing values of the S/C ratio in the feed are more clearly observable under other conditions of low temperature and space time values (Figs. S7 and S8). These results confirm that the excess of water in the feed (above the S/C ratio stoichiometric value of around 1.5) favors the SR and WGS reactions [30]. Nevertheless, it should be noted that too high S/C ratio in the feed (above the value of 6 used in this work) could involve counterproductive effects because (i) the competitive adsorption between water and oxygenates could decrease the catalytic activity to convert oxygenates [39,57], and (ii) the high energy consumption to generate steam decreases the process energy efficiency [36]. Moreover, Gao et al. [58] emphasize that an excess of steam could cool the active sites affecting the endothermic reactions.

The evolution with time on stream of the conversion (Fig. 4a) evidences that the increase in the S/C ratio in the feed attenuates the deactivation rate. Likewise, the decrease in the H_2 and CO_2 yield

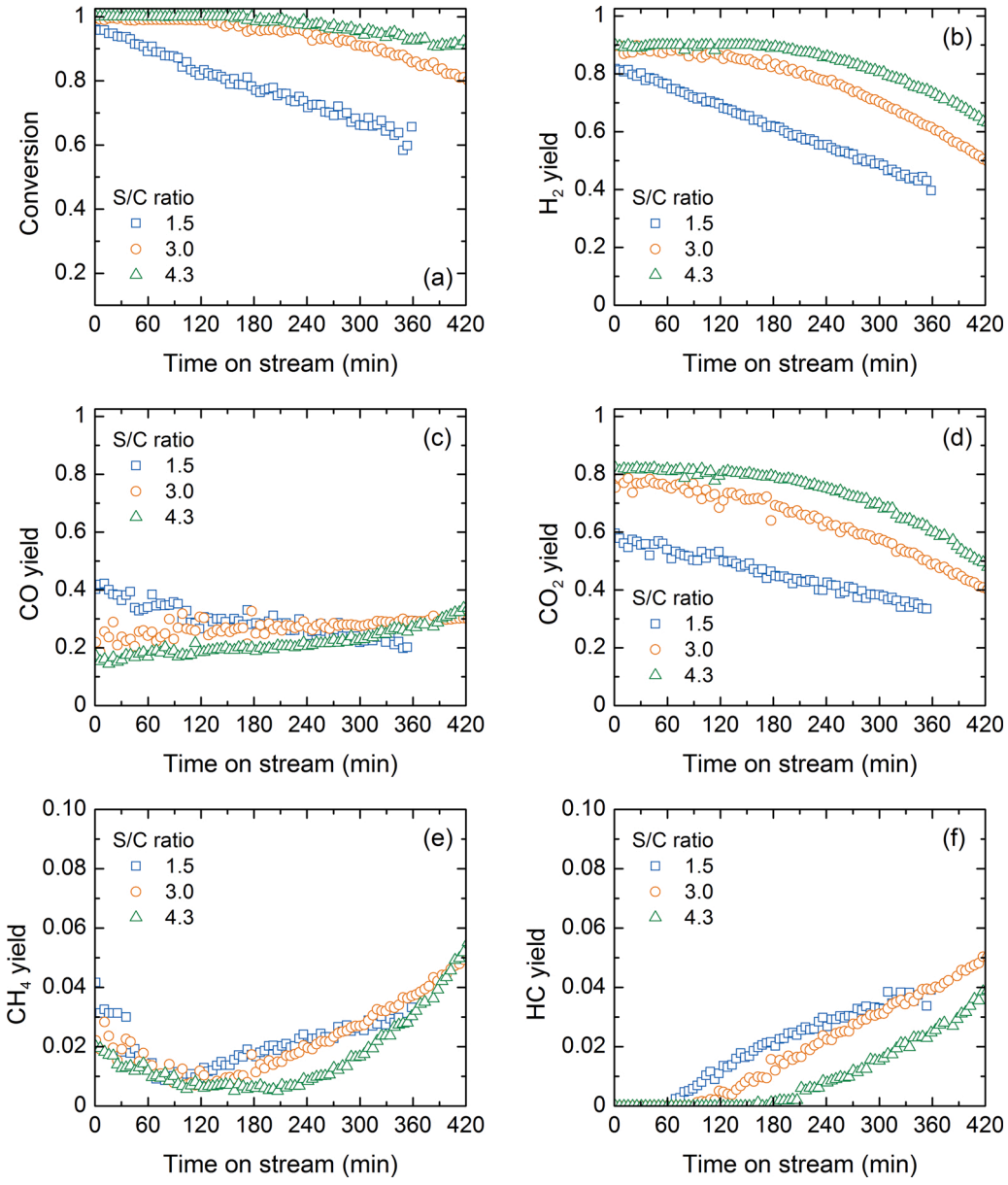

Fig. 4. Effect of steam/carbon (S/C) molar ratio in the feed on the evolution with time on stream of the conversion of oxygenates (a) and yield of H_2 (b), CO (c), CO_2 (d), CH_4 (e) and hydrocarbons (HC) (f). Reaction conditions: 700 °C; space time, 0.25 h.

(Figs. 4b and d, respectively) is attenuated and the increase in the HC yield (Fig. 4e) is slower, in line with the catalyst deactivation attenuation for the SR and WGS reactions. This behavior is also observed at other reaction conditions in Figs. S7 and S8. The explanation for these results lies in the well-established attenuation of the coke deposition by increasing the water concentration in the reaction medium [11]. The variable evolution with time on stream of the CO and CH_4 yield for different values of the S/C ratio in the feed in Figs. 4, S7 and S8 is a consequence of the different extent of the formation and disappearance reactions of these intermediate compounds, as previously commented for the effect of temperature and space time. Thus, the yield of CO decreases with time on stream when it is mainly a final product in the reaction scheme (S/C ratio = 1.5, when the WGS reaction is not promoted), it remains constant when it behaves as an intermediate product (S/C ratio = 3) and slightly increases when it behaves as a primary product in the reaction scheme (S/C ratio = 6, when the WGS reaction is highly promoted). In the conditions of Fig. 4, corresponding to a high space time value, the CH_4 yield passes through a minimum with time on stream, as previously explained, which is reached at higher values of time on stream for a high S/C ratio, due to the attenuation of the deactivation caused by the excess of water.

3.2. Characterization of used catalysts and coke deposits

The results in the previous section showed that the severity in the deactivation of the $NiAl_2O_4$ spinel derived catalyst depends on the reaction conditions. In this section, we explored the plausible causes of deactivation (sintering of Ni crystals and the deposition of coke on the catalyst surface) by characterizing the used catalysts with different techniques (XRD, TPO, XPS, EDS, SEM and Raman spectroscopy). The used catalysts in the experiments with variable temperature (Fig. 2) are denoted as SRB-600, SRB-650 and SRB-700; with variable space time (Fig. 3) as SRB-0.075, SRB-0.15 and SRB-0.25, and; with variable S/C ratio in the feed (Fig. 4) as SRB-1.5, SRB-3.0 and SRB-4.3.

3.2.1. Structural analysis of used catalysts

The structural properties of the used catalysts were determined using XRD analysis with the purpose of assessing the degree of sintering of Ni crystals and the crystalline state of coke deposits. Fig. 5 shows the XRD patterns of the fresh (reduced) and used catalysts at variable reaction temperature (Fig. 5a), variable space time (Fig. 5b) and variable S/C ratio in the feed (Fig. 5c). The used catalysts show diffraction peaks similar to those of the fresh (reduced) catalyst, indicating the presence of phases of Al_2O_3 (2θ = 37.6, 45.8 and 67.0°) and Ni crystals (2θ = 44.7 and 52.0°). The average size of Ni crystals of the fresh (reduced) and used catalysts (Table 3) was calculated from the diffraction peak at 2θ = 52.0° by using the Scherrer equation [26]. The estimated value is 13.0 nm for the fresh (reduced) catalyst and slightly increases for the used catalysts in the range of 13.0–17.9 nm. These slight changes in the average size of Ni crystals show no evidence of a noticeable sintering phenomenon of Ni crystals, and therefore we rule out this as the cause responsible for catalyst deactivation at the reaction conditions used in this work.

The XRD patterns of the used catalysts also provide information on the coke deposits. The used catalyst of the experiment carried out at 700 °C (SRB-700 in Fig. 5a) shows a diffraction peak at 2θ = 26.3−26.6° that corresponds to crystalline carbon structures [22], whereas this peak does not appear for the experiments carried out at 600 and 650 °C. This peak is rather broad and with low intensity indicating the poor crystallinity of such structures and therefore the major amorphous nature of coke. Nevertheless, the increase in the space time at 700 °C (Fig. 5b) increases the intensity of this diffraction peak, which suggests the presence of more crystalline carbon structures. On the other hand, increasing the S/C ratio in the feed at 700 °C (Fig. 5c) does not affect the intensity of this diffraction peak.

Consequently, these results evidence that the coke crystallinity is affected by reaction conditions, whereas the sintering of Ni crystals is not significant within the studied range of reaction conditions.

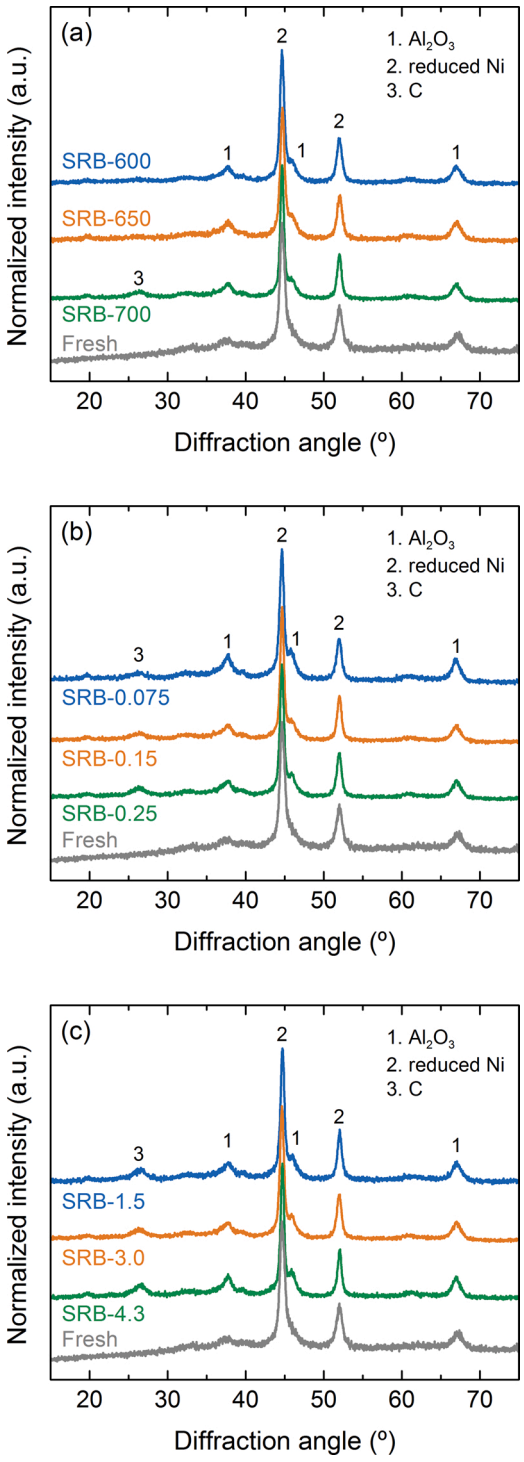

Fig. 5. XRD patterns of the used catalysts at different values of reaction temperature (a), space time (b) and steam/carbon (S/C) ratio in the feed (c). Used catalyst obtained at the conditions indicated in Figs. 2–4, respectively.

3.2.2. Coke combustion

The combustion characteristics and quantification of coke deposits on the catalyst surface were determined using TPO analysis. Fig. 6 shows the TPO profiles of the coke deposits on the used catalysts at variable reaction temperature (Fig. 6a), space time (Fig. 6b) and S/C ratio in the feed (Fig. 6c). Additionally, Figs. S9–S11 show the TPO profiles of coke

Table 3
Average size of Ni crystals, content (C_C) and average deposition rate (r_C) of coke for the experiments corresponding to Figs. 2–4.

T, °C	[a]Ni crystal size, nm	[b]C_C, mg g^{-1}	[c]r_C, mg g^{-1} min^{-1}
Fresh catalyst	13.0	-	-
SRB-600	13.0	141	0.987
SRB-650	13.0	93.0	1.25
SRB-700	16.2	143	0.807
SRB-0.075	13.5	112	3.17
SRB-0.15	16.2	143	0.807
SRB-0.25	15.9	160	0.510
SRB-1.5	16.1	138	0.877
SRB-3.0	15.9	160	0.510
SRB-4.3	17.9	175	0.541

[a] Calculated from the diffraction peak at 2θ = 52.0° using the Scherrer equation.
[b] Calculated from TPO profiles (area under the curve).
[c] Calculated as the ratio between the coke content and the half lifetime (determined from the experimental data of conversion).

formed in the experiments described in Figs. S3–S8. The TPO profiles show two ranges of coke combustion temperature, corresponding to two coke fractions: one range below 500 °C (combustion of coke I) and another above 500 °C (coke II).

As seen in Fig. 6a coke formed at 600 °C is predominantly coke I, with little presence of coke II. In contrast, coke on the catalysts used at 650 and 700 °C is mostly coke II. Likewise, coke on the catalysts used at 700 °C at different space time values (Fig. 6b) and S/C ratio values in the feed (Fig. 6c) is predominantly coke II. The results presented in Figs. S9–S11 for other reaction conditions confirm that the reaction temperature is the variable that determines the formation of coke I or coke II. The former type is preferentially formed in all the experiments with a reaction temperature of 600 °C, whereas the latter type is predominantly present in all the experiments with a reaction temperature equal or above 650 °C.

Table 3 summarizes the results of coke content on the used catalysts and the average deposition rate determined from the TPO profiles (Fig. 6). The average deposition rate was calculated as the ratio between the coke content and the half lifetime (determined from the experimental data of conversion). The analysis of the effect of temperature reveals that the minimum coke content (93.0 mg g^{-1}) is reached at 650 °C, but with a maximum deposition rate (1.25 mg g^{-1} min^{-1}), which is coherent with the faster deactivation at this intermediate reaction temperature (Fig. 2). Furthermore, the coke content slightly increases with increasing space time values, whereas the average coke deposition rate noticeable decreases. Likewise, the increase in the S/C ratio in the feed increases the coke content, but it decreases the average coke deposition because a high S/C ratio favors the coke gasification (Eq. (10)) and SR reactions (Eqs. (1),(5) and (6)). The results for the average deposition rate of coke are coherent with the effect of reaction conditions on the deactivation rate observed in Figs. 2–4: high values at 650 °C and with decreasing values of the space time and S/C ratio in the feed. Nevertheless, the values of coke content do not explain the deactivation rate due to the different duration of the reactions (higher duration when the deactivation is slower).

The presence of two coke fractions in the TPO profiles is commonly found in the used catalysts of the SR of oxygenates. There are two hypotheses to explain this phenomenon. One holds that coke I is deposited on or nearby the metal surface (even encapsulating the metal sites) and its combustion is catalyzed by metal sites, resulting in lower combustion temperature values, whereas coke II is presumably associated with deposits on the support, whose combustion is not catalyzed [20,21,27,44]. Another hypothesis holds that the presence of two different combustion temperature values may be attributable to the different coke natures based on the formation of amorphous carbon (burning at low temperature) and carbon filaments or graphitic structures (burning at high temperature) [59,60].

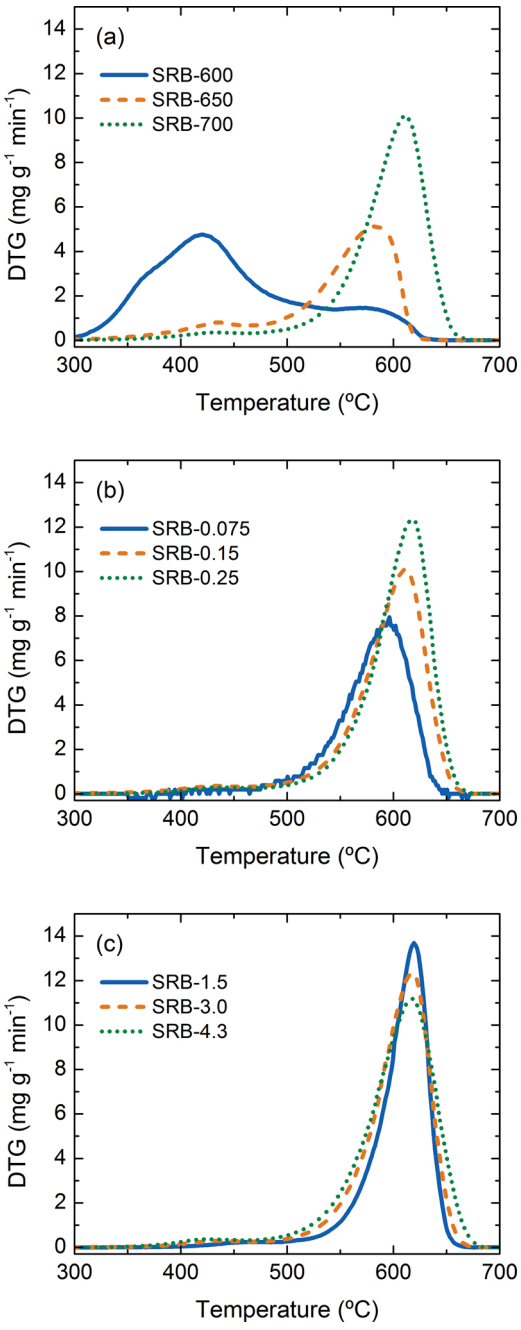

Fig. 6. TPO profiles of the used catalysts at different values of reaction temperature (a), space time (b) and steam/carbon ratio in the feed c). Used catalyst obtained at the conditions indicated in Figs. 2–4, respectively.

These results reveal that the reaction temperature is the most relevant variable affecting the coke nature or location on the catalyst surface, and consequently the catalyst deactivation. Therefore, we further analyze the used catalyst samples corresponding to different reaction temperature values using other analysis techniques (XPS, SEM or SEM-EDS, and Raman spectroscopy) with the purpose of elucidating the coke type nature and location.

3.2.3. *Surface composition*

The atomic composition of the surface species present on the fresh catalyst and used catalysts at different reaction temperature values (corresponding to the experiments described in Fig. 2) was determined using XPS. Table 4 summarizes the atomic composition determined using XPS in a 1 × 3 mm area and at a thin superficial layer of

Table 4
Atomic composition (in %) determined using XPS analysis of fresh (reduced) and catalysts used at different reaction temperature, and results of carbon spectra.

Components	Fresh	SRB-600	SRB-650	SRB-700
Carbon	–	94.2	98.3	98.6
Oxygen	60.0	3.90	1.70	1.40
Aluminum	34.8	1.90	N.D.	N.D.
Nickel	5.20	N.D.	N.D.	N.D.
Deconvolution of carbon spectrum:				
sp^2: C—C, C—H		61.70	65.29	62.47
sp^3: C—C, C—H		11.93	11.69	12.77
C—O		8.07	8.28	8.93
O—C═O		6.35	6.18	6.74
π-π satellite		6.13	6.88	7.70

approximately 1−2 nm of each used catalyst sample. The results indicate the presence of O, Al and Ni atoms on the surface of the fresh catalyst, with 5.20 % (13.4 wt%) of Ni atoms on the particle surface, and considering that the stoichiometric content of Ni is 33 wt%, we infer that Ni is predominantly located at a higher concentration inside the particles (undetectable by XPS).

The atomic composition of the surface of the used catalysts evidences the severity of coke deposition, leading to the total coverage of the catalyst particle surface with coke at 650 and 700 °C, as no Al or Ni are detected. Likewise, this analysis evidences that the support surface of the catalyst used at 600 °C is less covered with coke than at high temperature values, which may be related to the preferential location of coke inside the particle where there is a higher Ni concentration. O atoms are also present on the surface of the used catalysts, which are attached to C or Al atoms. At 650 and 700 °C, O atoms are combined only with C atoms since there is no evidence of Al on the surface of these samples, whereas the O atoms are combined with both C and Al atoms on the surface of the catalyst used at 600 °C. The oxygenated nature of coke indicates that coke is probably formed through the decomposition of oxygenates (Eq. (4)).

The carbon spectra of the surface of the used catalysts (Fig. S12) provide information on the carbon species according to how a C atom interacts with surrounding atoms. Each spectrum was corrected by the Shirley baseline method and deconvoluted into five main peaks (excluding the contribution of SiC seen at 282.8 eV). The results of these deconvolutions are shown in Table 4. The peaks are commonly assigned to [22,61–65]: C attached to another C or a H atom (C—C or CH—) at 284.6 eV; C atom attached to a C atom that is attached to an O atom (C—COR) at 285.5 eV; C atom attached to an O atom (C═O, CO—X) at 286.6 eV; C atom attached to two O atoms (O═CO—) at 288.6 eV; and satellite of the π-π interactions at 291.0 eV. Another plausible interpretation for these spectra is based on the presence of different carbon hybridizations (sp^2 and sp^3) [63,64]: the C atoms attached to H or C atoms with sp^2 or sp^3 hybridization have binding energies of 284.6 or 285.5 eV, respectively, whereas those attached to O atoms with sp^3 or sp^2 hybridization have binding energies of 286.6 or 288.6 eV, respectively. As seen in Table 4, the results do not show a clear trend of the different sp^2/sp^3 hybridized or oxygenated carbon species with the reaction temperature, instead they are similar. On the other hand, we can roughly estimate a relative portion of aromatic carbon based on the satellite peak of π-π interactions, indicating that the aromatic species (aromaticity of coke deposits) increase with increasing reaction temperature values.

3.2.4. Coke location

The XPS results gave clues on the possible preferential coke location and we further evaluated this using BSD-SEM and combined SEM-EDS analyses for the experiments described in Fig. 2. Fig. 7 shows the BSD-SEM images of the fresh and used catalysts at different reaction temperature values. These images provide information on the elements

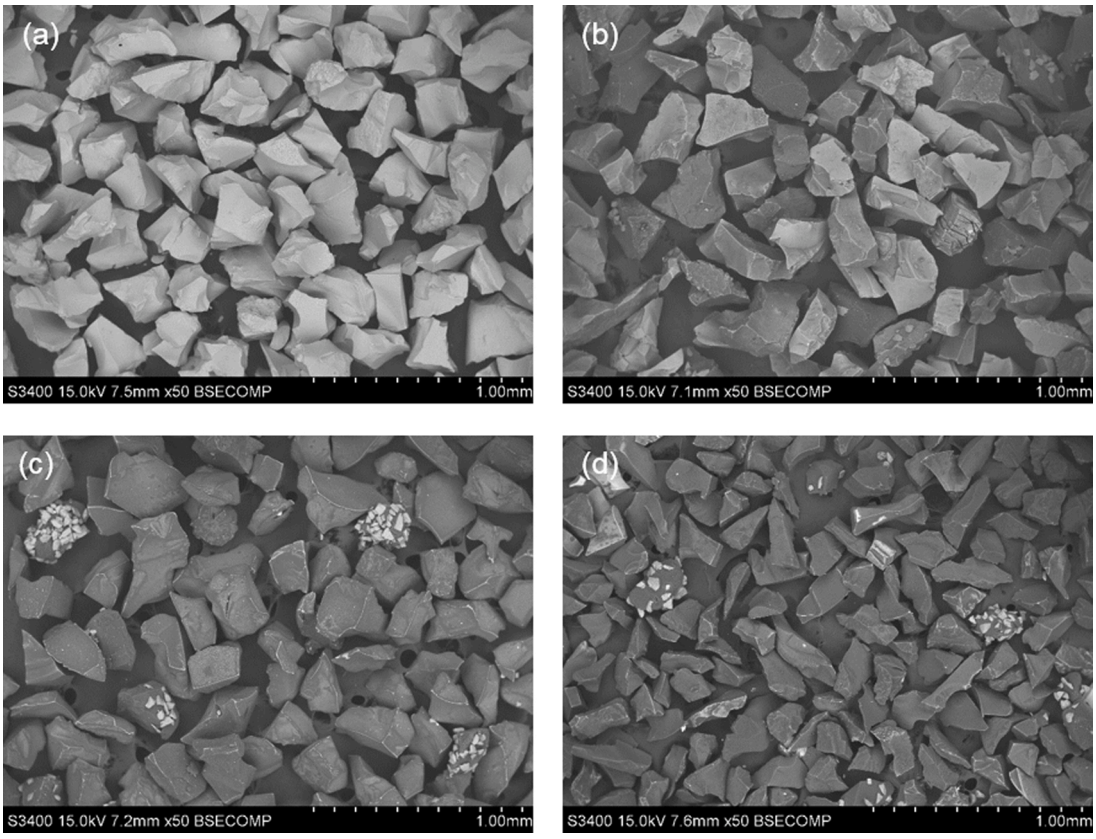

Fig. 7. BSD-SEM images of the fresh catalyst (a) and used catalysts at 600 °C (b), 650 °C (c) and 700 °C (d). Used catalyst obtained at the conditions indicated in Fig. 2.

present on the particle surface based on the fact that the brightness depends on the atomic number of the elements when using a BSD [20]. Thus, the image brightness increases when the abundance of heavy elements (Ni or Al accounting for the catalyst phases) increases and decreases when the abundant of light elements (C accounting for coke deposits) increases.

The particles of the fresh catalyst (Fig. 7a) show the brightest color indicating the absolute presence of Al and Ni on the external surface. On the other hand, the particles of the catalyst used at 600 °C (Fig. 7b) are grey-colored with two different tones, making evident the presence of two different particles. On the other hand, the particles of the catalysts used at 650 (Fig. 7c) and 700 °C (Fig. 7d) show the darkest color with a high uniformity, indicating the predominant presence of C on the external surface. The non-uniformity of the particles of the catalyst used at 600 °C indicates the different extent of coke deposition on the external surface of the catalyst particles. Thus, the brightest particles would have less coke deposits on the external surface of the catalyst particles. These observations make evident that coke is preferentially deposited on the internal surface of the catalyst particle at 600 °C where most of Ni crystals are located, whereas coke is deposited on the external surface of the catalyst at 650 and 700 °C.

The analysis of coke location was complemented using SEM-EDS. Fig. 8 shows the SEM images for the used catalysts and the corresponding maps of elements measured with EDS. Fig. S13 shows a similar

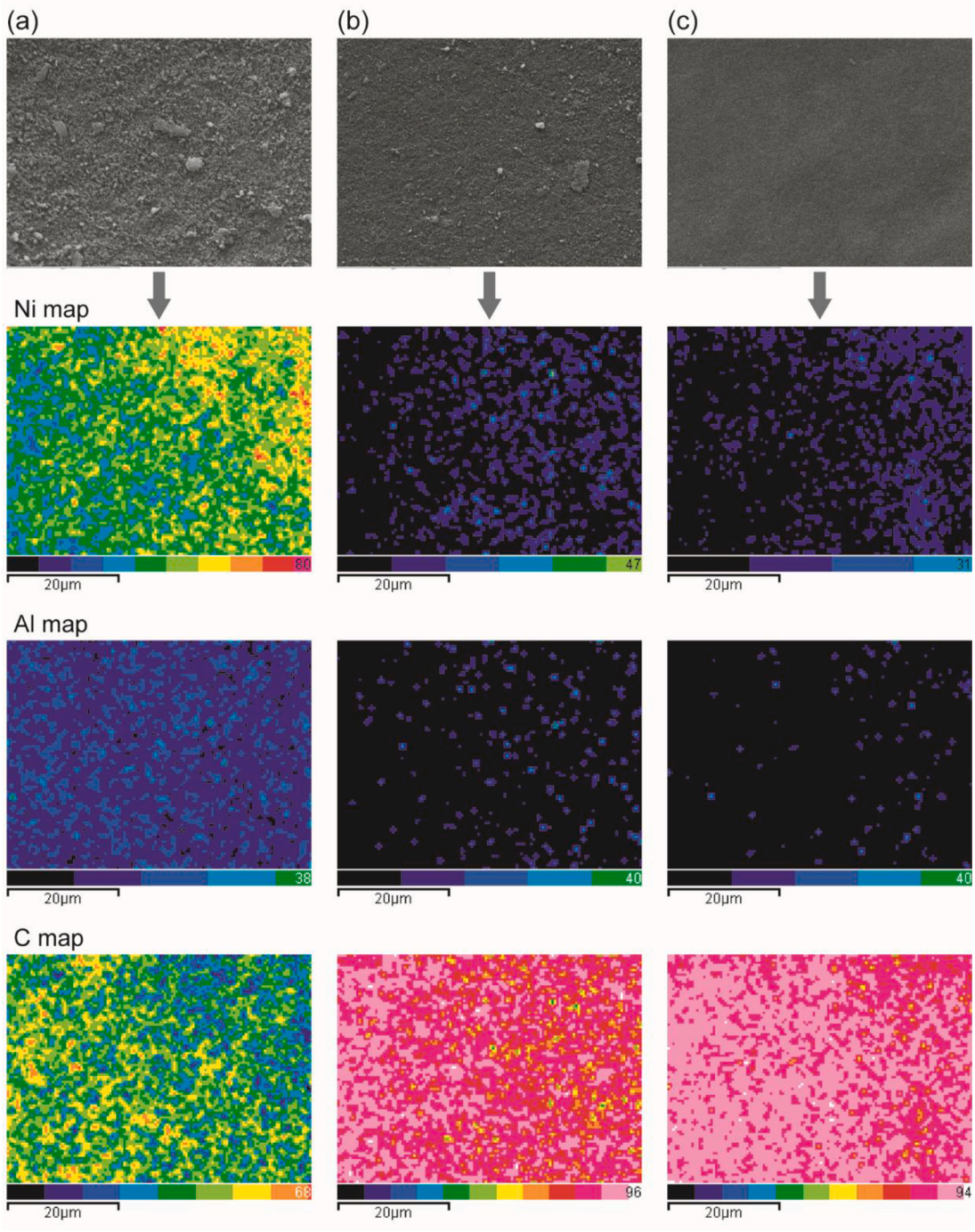

Fig. 8. SEM images and maps of elements detected by EDS of the used catalysts at 600 °C (a), 650 °C (b) and 700 °C (c). Used catalyst obtained at the conditions indicated in Fig. 2.

analysis for the fresh catalyst. The C map reveals an extremely high coke content on the surface of the catalysts used at 650 and 700 °C, blocking the surface of Ni crystals and Al_2O_3. Nevertheless, the Al and Ni maps of the catalyst used at 600 °C evidence that part of the surfaces of Al_2O_3 and Ni sites, respectively, are free of coke. Additionally, when comparing the Ni and C maps of the catalyst used at 600 °C, it is evident that the zones with the highest abundance of coke correspond to zones with lower abundance of Ni crystals, presumably indicating that coke is deposited on Ni sites and this hinders the detection of Ni. The low abundance of Ni on the surface of the catalysts used at 650 and 700 °C (in agreement with XPS results in Table 2) should be attributed to high abundance of coke on the surface of these used catalysts, that hinders the detection of Ni. Besides, the majority of the Ni crystals would be presumably located inside the catalyst particle, according to the XPS analysis results.

3.2.5. Coke morphology

Fig. 9 shows the SEM images of the fresh catalyst and catalysts used at different reaction temperature values corresponding to the experiments described in Fig. 2. Upon analyzing various particles in each catalyst sample, we observed a high degree of uniformity of the surface morphology for the fresh catalyst (Fig. 9a) and catalysts used at 650 °C (Fig. 9d) and 700 °C (Fig. 9f). On the other hand, two different surface morphologies can be distinguished for the particles of the catalyst used at 600 °C (Figs. 9b and 9c), which is related to the two different particles observed using BSD-SEM. The typical particles of the fresh catalyst (Fig. 9a) show a uniform granular-like texture, corresponding to that of porous alumina phases [66]. The particles of the used catalysts show coke deposits in the form of carbon filaments on the external surface, with different characteristics according to the reaction temperature.

The filamentous nature of coke has been observed in the SRB on other Ni catalysts [22,45] and it is also usually observed in the SR of oxygenates on Ni catalysts [46,67]. However, the carbon filaments

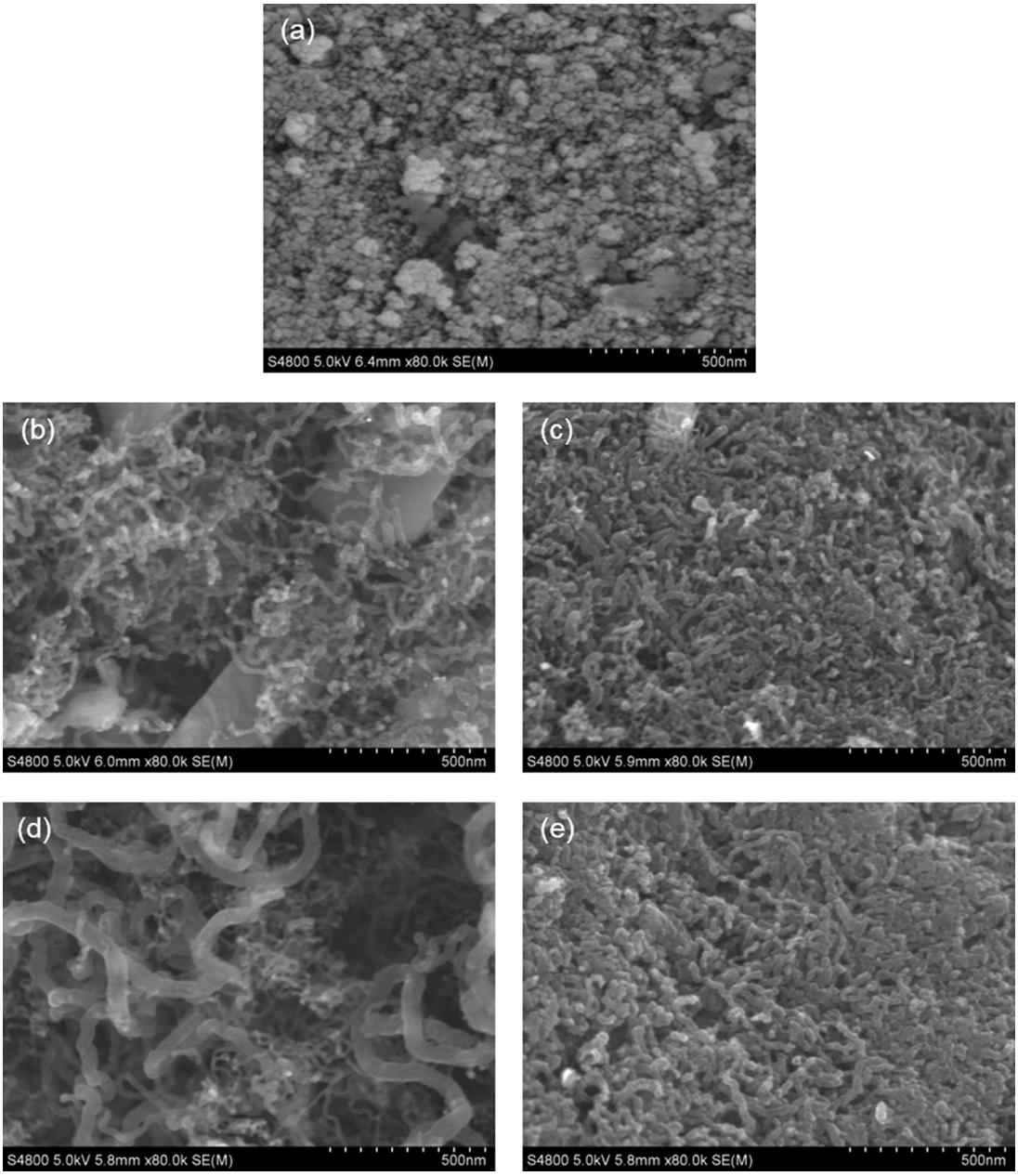

Fig. 9. SEM images of the fresh catalyst (a) and used catalysts at 600 °C (b, c), 650 °C (d) and 700 °C (e). Used catalyst obtained at the conditions indicated in Fig. 2.

observed in this work are different from the typical carbon filaments observed on other catalysts in terms of being smaller with different lengths and thicknesses. The filaments formed at 600 °C have different characteristics, being thinner and looser in the brightest particles, and thicker and more abundant in the darkest particles. The brightest particles also show a low abundance of carbon filaments as evidenced in Fig. S14 at a lower zoom, in which the catalyst surface can be seen in the SEM image with an incipient formation of filaments. Besides, some filaments look compacted in the darkest particles, indicating the deposition of another carbon phase in between them. At 650 °C, the size of filaments is heterogeneous, some of them being notoriously larger than the ones observed on the other samples. At 700 °C, the filaments tend to be more ordered (compacted) with more uniform diameters, which indicates the deposition of other carbon phase in between the filaments. This second carbon phase may correspond to pyrolytic carbon with a graphite-like structure [20], which explains the slight crystallinity observed in the XRD patterns for the catalysts used at 700 °C. In contrast, the carbon phase deposited in between filaments at 600 °C is amorphous because the XRD patterns show no crystallinity and the TPO profiles give a low combustion temperature.

Comparing these results with those of deactivation (Fig. 2), the slower deactivation observed at 600 °C can be related to the lower abundance and diameter of the carbon filaments in some particles, evidencing an incipient formation of carbon filaments. In order to prove this relation, we carried out an additional experiment at 600 °C and at conditions similar to those used in the experiments described in Fig. 2 until observing complete catalyst deactivation after 13 h on stream. Afterwards, the corresponding used catalyst was analyzed using SEM analysis. The image (Fig. 10) shows that the abundance and diameter of the carbon filaments are higher than those at 4.5 h on stream (Fig. 7b), with a major presence of amorphous carbon deposited in between the filaments. Interestingly, the used catalyst at 600 °C after 13 h on stream (complete deactivation) only shows the presence of coke I (Fig. S15), confirming the deposition of amorphous carbon in between the filaments.

These results evidence that the increase in the temperature (between 600 and 650 °C) favors the growth of carbon filaments on the Ni sites. The increase in the carbon filament size at 650 °C may detach Ni crystals from the support according to the tip-growth mechanism [46], causing an encapsulation of the Ni crystals (inside the carbon filament) and the direct deposition of these carbon filaments on the support surface blocking the access to the support sites. However, increasing the temperature up to 700 °C slightly prevents the growth of carbon filaments, possibly by favoring coke gasification reactions (as Eq. (10)), but promotes the formation and deposition of a graphitic-like carbon phase apparently on the support surface that causes deactivation.

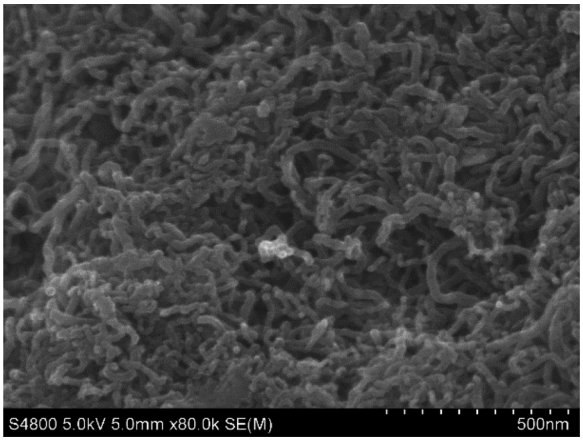

Fig. 10. SEM image of the used catalyst at 600 °C after 13 h on stream. Used catalyst obtained at the conditions similar to those indicated in Fig. 2.

3.2.6. Coke structure

Fig. 11 shows the Raman spectra of the catalysts used at different reaction temperature values corresponding to the experiments described in Fig. 2. All the spectra show similar features: two first-order resonance bands with maxima at ~1337–1344 cm^{-1} (sp^2 hybridized carbons in aromatic rings named D band) and ~1597 cm^{-1} (sp^2 hybridized carbons in aromatic rings and olefins named G band) and second-order bands with modulated bumps in the 2250–3250 cm^{-1} region (Fig. S16) [68]. The D and G bands and the modulated-bumped bands at 2250–3250 cm^{-1} are characteristic of several carbon structures, and based on our previous analysis of coke deposits (XRD and SEM analyses), these Raman features may correspond to those of carbon filaments with a high degree of amorphousness provided by the atypical lengths in comparison to those of typical carbon nanotubes.

To better evaluate the Raman parameters, we deconvoluted each spectrum in four Lorentzian bands with positions at 1180 cm^{-1} (possible assigned to sp^3 hybridized carbons), 1337–1344 cm^{-1} (D band), 1490 cm^{-1} (assigned to phases of amorphous carbon) and 1597 cm^{-1} (G band) [69]. The deconvolution results listed in Table 5 show that the position of the D band and the relative intensity of the D and G bands (I_D/I_G) increase with increasing reaction temperature values. Likewise, the full width at haft maximum (FWHM) of the D band is smaller for the used catalyst at 700 °C than for the used catalysts at 650 or 600 °C, whereas there is not a clear trend for the FWHM of the G band.

The interpretation of the Raman spectra is not straightforward neither absolute, since our results indicate the presence of carbon filaments with a high degree of amorphousness. Thus, an appropriate approach is to consider the interpretation for amorphous carbons proposed by Ferrari and Robertson [68], in which the increase in the I_D/I_G ratio indicates an increase in the size of ordered domains (graphitization). The deconvolution parameters obtained in this work indicate that the coke deposits would have a major degree of order or graphitization at 700 and 650 °C than at 600 °C, which is well correlated with the combustion temperature ranges observed in the TPO profiles. These results also correlate well with our XRD and SEM analyses, making evident that the increase in carbon filament size at 650 °C and the deposition of pyrolytic carbon in between carbon filaments (with a crystalline phase) at 700 °C increase the graphitization degree of coke.

4. Conclusions

The results confirm the high activity and H_2 selectivity of the $NiAl_2O_4$ spinel derived catalyst for the SR of bio-oil at moderate temperature (600–700 °C), reaching a hydrogen yield of 90 % with a low value of space time. The sintering of Ni crystals is negligible at these reaction conditions, and the catalyst undergoes deactivation by coke deposition. The increase in the space time (0.038–0.25 h) and steam/

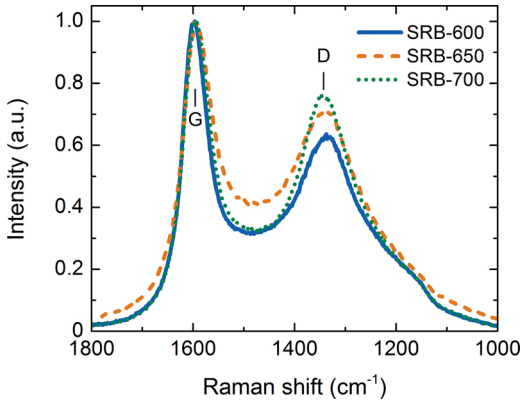

Fig. 11. Raman spectra of the used catalysts at 600 °C, 650 °C and 700 °C. Used catalyst obtained at the conditions indicated in Fig. 2.

Table 5
Deconvolution parameters of the Raman spectra of the used catalysts at different reaction temperature values.

Parameter	SRB-600	SRB-650	SRB-700
D position (cm^{-1})	1337	1342	1344
$FWHM_D$ (cm^{-1})	154	157	139
$FWHM_G$ (cm^{-1})	53	61	56
I_D/I_G ratio	0.69	0.76	0.81

carbon molar ratio in the feed (1.5–6) contributes to attenuate the coke deposition, whose nature and location mainly depends on the reaction temperature.

Coke is composed of short and heterogeneous filaments and the structure depends on the reaction temperature. The filaments formed at 600 °C are thinner and loose, preferentially located on the Ni sites inside the catalyst particle, whereas those formed at 650 or 700 °C are larger and more developed/structured causing their deposition over the catalyst support. Furthermore, the deposition of amorphous and pyrolytic carbon phases in between the filaments observed at 600 and 700 °C, respectively, also contributes to catalyst deactivation.

The selection of the reaction temperature in the 600−700 °C range greatly affects the catalyst stability with a complex effect. Thus, the increase in the temperature favors the coke formation and gasification, promoting the formation of a more structured coke that tends to be deposited on the catalyst support and it is more difficult to gasify (particularly at 650 °C). Consequently, the reaction should be carried out at 600 °C to provide a more efficient availability of catalytic sites (Ni and alumina sites) for the reactants.

These results are of interest to progress in the preparation of active, stable and regenerable catalysts, based on $NiAl_2O_4$ spinel, for their use on a larger scale at 600 °C in the reforming of raw bio-oil.

CRediT authorship contribution statement

Naiara García-Gómez: Methodology, Investigation, Data curation. **José Valecillos:** Conceptualization, Investigation, Writing - original draft, Visualization. **Aingeru Remiro:** Methodology, Investigation, Data curation. **Beatriz Valle:** Conceptualization, Methodology, Supervision. **Javier Bilbao:** Conceptualization, Writing - review & editing, Visualization. **Ana G. Gayubo:** Conceptualization, Writing - review & editing, Visualization, Supervision, Funding acquisition.

Declaration of Competing Interest

The authors report no declarations of interest.

Acknowledgments

This work was carried out with the financial support of the Department of Education, Universities and Investigation of the Basque Government (IT1218-19), theEuropean Commission(HORIZON H2020-MSCA RISE 2018. Contract No. 823745), the Ministry of Economy and Competitiveness of the Spanish Government jointly with European Regional Development Funds(AEI/FEDER, UE) (Projects CTQ2015-68883-R and RTI2018-100771-B-I00), and PhD grant (BES-2016-078132) for N. García-Gómez. The authors thank for technical and human support provided by SGIker (UPV/EHU/ ERDF, EU).

Appendix A. Supplementary data

Supplementary material related to this article can be found, in the online version, at doi:https://doi.org/10.1016/j.apcatb.2021.120445.

References

[1] Z. Abdin, A. Zafaranloo, A. Rafiee, W. Mérida, W. Lipiński, K.R. Khalilpour, Hydrogen as an energy vector, Renew. Sustain. Energy Rev. 120 (2020), 109620, https://doi.org/10.1016/j.rser.2019.109620.
[2] A. Kumar, J.P. Chakraborty, R. Singh, Bio-oil: the future of hydrogen generation, Biofuels 8 (2017) 663–674, https://doi.org/10.1080/17597269.2016.1141276.
[3] H. Nazir, N. Muthuswamy, C. Louis, S. Jose, J. Prakash, M.E.M. Buan, C. Flox, S. Chavan, X. Shi, P. Kauranen, T. Kallio, G. Maia, K. Tammeveski, N. Lymperopoulos, E. Carcadea, E. Veziroglu, A. Iranzo, A.M. Kannan, Is the H_2 economy realizable in the foreseeable future? Part III: H_2 usage technologies, applications, and challenges and opportunities, Int. J. Hydrogen Energy 45 (2020) 28217–28239, https://doi.org/10.1016/j.ijhydene.2020.07.256.
[4] T. Shan, S. Anto, T. Mathimani, K. Brindhadevi, A. Pugazhendhi, Upgrading of bio-oil from thermochemical conversion of various biomass – mechanism, challenges and opportunities, Fuel 287 (2021), 119329, https://doi.org/10.1016/j.fuel.2020.119329.
[5] W. Nabgan, T.A. Tuan Abdullah, R. Mat, B. Nabgan, Y. Gambo, M. Ibrahim, A. Ahmad, A.A. Jalil, S. Triwahyono, I. Saeh, Renewable hydrogen production from bio-oil derivative via catalytic steam reforming: an overview, Renew. Sustain. Energy Rev. 79 (2017) 347–357, https://doi.org/10.1016/j.rser.2017.05.069.
[6] R. Kumar, V. Strezov, Thermochemical production of bio-oil : a review of downstream processing technologies for bio-oil upgrading, production of hydrogen and high value-added products oil in water, Renew. Sustain. Energy Rev. 135 (2021), 110152, https://doi.org/10.1016/j.rser.2020.110152.
[7] L. Dai, Y. Wang, Y. Liu, C. He, R. Ruan, Z. Yu, L. Jiang, Z. Zeng, Q. Wu, A review on selective production of value-added chemicals via catalytic pyrolysis of lignocellulosic biomass, Sci. Total Environ. 749 (2020), 142386, https://doi.org/10.1016/j.scitotenv.2020.142386.
[8] N. Gao, K. Kamran, C. Quan, P.T. Williams, Thermochemical conversion of sewage sludge: a critical review, Prog. Energy Combust. Sci. 79 (2020), 100843, https://doi.org/10.1016/j.pecs.2020.100843.
[9] B. Valle, N. García-Gómez, A. Arandia, A. Remiro, J. Bilbao, A.G. Gayubo, Effect of phenols extraction on the behavior of Ni-spinel derived catalyst for raw bio-oil steam reforming, Int. J. Hydrogen Energy 44 (2019) 12593–12603, https://doi.org/10.1016/j.ijhydene.2018.12.057.
[10] Q. Xu, P. Feng, K. Huang, S. Xin, T. Wei, L. Liao, Y. Yan, Research of the combined reforming of bio-oil model compound for hydrogen production, Environ. Prog. Sustain. Energy 39 (2020) 1–9, https://doi.org/10.1002/ep.13320.
[11] Z. Zhao, Y.A. Situmorang, P. An, N. Chaihad, J. Wang, X. Hao, G. Xu, A. Abudula, G. Guan, Hydrogen production from catalytic steam reforming of bio-oils: a critical review, Chem. Eng. Technol. 43 (2020) 625–640, https://doi.org/10.1002/ceat.201900487.
[12] H.D. Setiabudi, M.A.A. Aziz, S. Abdullah, L.P. Teh, R. Jusoh, Hydrogen production from catalytic steam reforming of biomass pyrolysis oil or bio-oil derivatives: a review, Int. J. Hydrogen Energy 45 (2020) 18376–18397, https://doi.org/10.1016/j.ijhydene.2019.10.141.
[13] L. Santamaria, G. Lopez, A. Arregi, M. Amutio, M. Artetxe, J. Bilbao, M. Olazar, Stability of different Ni supported catalysts in the in-line steam reforming of biomass fast pyrolysis volatiles, Appl. Catal. B Environ. 242 (2019) 109–120, https://doi.org/10.1016/j.apcatb.2018.09.081.
[14] N. Gao, J. Salisu, C. Quan, P. Williams, Modified nickel-based catalysts for improved steam reforming of biomass tar: a critical review, Renew. Sustain. Energy Rev. 145 (2021), 111023, https://doi.org/10.1016/j.rser.2021.111023.
[15] H. Tian, C. Pei, Y. Wu, S. Chen, Z. Zhao, J. Gong, Tunable metal-oxide interaction with balanced Ni°/Ni^{2+} sites of $Ni_xMg_{1-x}O$ for ethanol steam reforming, Appl. Catal. B Environ. 293 (2021), 120178, https://doi.org/10.1016/j.apcatb.2021.120178.
[16] W. Zhao, S.J. Carey, Z. Mao, C.T. Campbell, Adsorbed hydroxyl and water on Ni (111): heats of formation by calorimetry, ACS Catal. 8 (2018) 1485–1489, https://doi.org/10.1021/acscatal.7b04041.
[17] X. Hu, G. Lu, Comparative study of alumina-supported transition metal catalysts for hydrogen generation by steam reforming of acetic acid, Appl. Catal. B Environ. 99 (2010) 289–297, https://doi.org/10.1016/j.apcatb.2010.06.035.
[18] S. Isarapakdeetham, P. Kim-Lohsoontorn, S. Wongsakulphasatch, W. Kiatkittipong, N. Laosiripojana, J. Gong, S. Assabumrungrat, Hydrogen production via chemical looping steam reforming of ethanol by Ni-based oxygen carriers supported on CeO_2 and La_2O_3 promoted Al_2O_3, Int. J. Hydrogen Energy 45 (2019) 1477–1491, https://doi.org/10.1016/j.ijhydene.2019.11.077.
[19] A. Mehdad, N. Gould, B. Xu, R. Lobo, Effect of steam and CO_2 in ethane activation on Zn-ZSM-5, Catal. Sci. Technol. 8 (2017) 358–366, https://doi.org/10.1039/C7CY01850A.
[20] A. Ochoa, J. Bilbao, A.G. Gayubo, P. Castaño, Coke formation and deactivation during catalytic reforming of biomass and waste pyrolysis products: a review, Renew. Sustain. Energy Rev. 119 (2020), 109600, https://doi.org/10.1016/j.rser.2019.109600.
[21] X. Hu, Z. Zhang, M. Gholizadeh, S. Zhang, C.H. Lam, Z. Xiong, Y. Wang, Coke formation during thermal treatment of bio-oil, Energy Fuels 34 (2020) 7863–7914, https://doi.org/10.1021/acs.energyfuels.0c01323.
[22] A. Ochoa, B. Aramburu, B. Valle, D.E. Resasco, J. Bilbao, A.G. Gayubo, P. Castaño, Role of oxygenates and effect of operating conditions in the deactivation of a Ni supported catalyst during the steam reforming of bio-oil, Green Chem. 19 (2017) 4315–4333, https://doi.org/10.1039/C7GC01432E.
[23] A. Kumar, A.S.K. Sinha, Comparative study of hydrogen production from steam reforming of acetic acid over synthesized catalysts via MOF and wet impregnation

methods, Int. J. Hydrogen Energy 45 (2020) 11512–11526, https://doi.org/10.1016/j.ijhydene.2020.02.097.
[24] A. Kumar, A.S.K. Sinha, Hydrogen production from acetic acid steam reforming over nickel-based catalyst synthesized via MOF process, Int. J. Hydrogen Energy 45 (2020) 24397–24411, https://doi.org/10.1016/j.ijhydene.2020.06.040.
[25] A. Arandia, A. Remiro, V. García, P. Castaño, J. Bilbao, A. Gayubo, Oxidative steam reforming of raw bio-oil over supported and bulk Ni catalysts for hydrogen production, Catalysts 8 (2018) 322, https://doi.org/10.3390/catal8080322.
[26] A. Remiro, A. Arandia, L. Oar-Arteta, J. Bilbao, A.G. Gayubo, Regeneration of $NiAl_2O_4$ spinel type catalysts used in the reforming of raw bio-oil, Appl. Catal. B Environ. 237 (2018) 353–365, https://doi.org/10.1016/j.apcatb.2018.06.005.
[27] A. Arandia, A. Remiro, B. Valle, J. Bilbao, A.G. Gayubo, Deactivation of Ni spinel derived catalyst during the oxidative steam reforming of raw bio-oil, Fuel 276 (2020), https://doi.org/10.1016/j.fuel.2020.117995.
[28] J. Du, J. Gao, F. Gu, J. Zhuang, B. Lu, L. Jia, G. Xu, Q. Liu, F. Su, A strategy to regenerate coked and sintered Ni/Al_2O_3 catalyst for methanation reaction, Int. J. Hydrogen Energy 43 (2018) 20661–20670, https://doi.org/10.1016/j.ijhydene.2018.09.128.
[29] C. Quan, N. Gao, H. Wang, H. Sun, C. Wu, X. Wang, Z. Ma, Ethanol steam reforming on Ni/CaO catalysts for coproduction of hydrogen and carbon nanotubes, Int. J. Energy Res. 43 (2019) 1255–1271, https://doi.org/10.1002/er.4365.
[30] C.T. Rodrigues, C.G. Alonso, G.D. Machado, T.L. de Souza, Optimization of bio-oil steam reforming process by thermodynamic analysis, Int. J. Hydrogen Energy 45 (2020) 28350–28360, https://doi.org/10.1016/j.ijhydene.2020.07.206.
[31] C. Montero, L. Oar-Arteta, A. Remiro, A. Arandia, J. Bilbao, A.G. Gayubo, Thermodynamic comparison between bio-oil and ethanol steam reforming, Int. J. Hydrogen Energy 40 (2015) 15963–15971, https://doi.org/10.1016/j.ijhydene.2015.09.125.
[32] S. Authayanun, D. Saebea, Y. Patcharavorachot, S. Assabumrungrat, A. Arpornwichanop, Optimal design of different reforming processes of the actual composition of bio-oil for high-temperature PEMFC systems, Int. J. Hydrogen Energy 42 (2017) 1977–1988, https://doi.org/10.1016/j.ijhydene.2016.10.125.
[33] A. Arregi, G. Lopez, M. Amutio, M. Artetxe, I. Barbarias, J. Bilbao, M. Olazar, Role of operating conditions in the catalyst deactivation in the in-line steam reforming of volatiles from biomass fast pyrolysis, Fuel. 216 (2018) 233–244, https://doi.org/10.1016/j.fuel.2017.12.002.
[34] J.O. Ighalo, A. George, Factor effects and interactions in steam reforming of biomass bio-oil, Chem. Pap. 74 (2020) 1459–1470, https://doi.org/10.1007/s11696-019-00996-3.
[35] K.A. Resende, C.N. Ávila-Neto, R.C. Rabelo-Neto, F.B. Noronha, C.E. Hori, Thermodynamic analysis and reaction routes of steam reforming of bio-oil aqueous fraction, Renew. Energy 80 (2015) 166–176, https://doi.org/10.1016/j.renene.2015.01.057.
[36] L. Landa, A. Remiro, R. De Torre, R. Aguado, J. Bilbao, G. Gayubo, Global vision from the thermodynamics of the effect of the bio-oil composition and the reforming strategies in the H_2 production and the energy requirement, Energy Convers. Manage. 239 (2021), 114181, https://doi.org/10.1016/j.enconman.2021.114181.
[37] S. Mahamulkar, K. Yin, P.K. Agrawal, R.J. Davis, C.W. Jones, A. Malek, H. Shibata, Formation and oxidation/gasification of carbonaceous deposits: a review, Ind. Eng. Chem. Res. 55 (2016) 9760–9818, https://doi.org/10.1021/acs.iecr.6b02220.
[38] A. Remiro, B. Valle, A.T. Aguayo, J. Bilbao, A.G. Gayubo, Operating conditions for attenuating Ni/La_2O_3-αAl_2O_3 catalyst deactivation in the steam reforming of bio-oil aqueous fraction, Fuel Process. Technol. 115 (2013) 222–232, https://doi.org/10.1016/j.fuproc.2013.06.003.
[39] C. Quan, S. Xu, C. Zhou, Steam reforming of bio-oil from coconut shell pyrolysis over Fe/olivine catalyst, Energy Convers. Manage. 141 (2017) 40–47, https://doi.org/10.1016/j.enconman.2016.04.024.
[40] J. Sehested, J.A.P. Gelten, I.N. Remediakis, H. Bengaard, J.K. Nørskov, Sintering of nickel steam-reforming catalysts: effects of temperature and steam and hydrogen pressures, J. Catal. 223 (2004) 432–443, https://doi.org/10.1016/j.jcat.2004.01.026.
[41] A. Arregi, G. Lopez, M. Amutio, I. Barbarias, L. Santamaria, J. Bilbao, M. Olazar, Kinetic study of the catalytic reforming of biomass pyrolysis volatiles over a commercial Ni/Al_2O_3 catalyst, Int. J. Hydrogen Energy 43 (2018) 12023–12033, https://doi.org/10.1016/j.ijhydene.2018.05.032.
[42] C. Montero, A. Remiro, B. Valle, L. Oar-Arteta, J. Bilbao, A.G. Gayubo, Origin and nature of coke in ethanol steam reforming and its role in deactivation of Ni/La_2O_3-αAl_2O_3 catalyst, Ind. Eng. Chem. Res. 58 (2019) 14736–14751, https://doi.org/10.1021/acs.iecr.9b02880.
[43] X. Li, Z. Zhang, L. Zhang, H. Fan, X. Li, Q. Liu, S. Wang, X. Hu, Investigation of coking behaviors of model compounds in bio-oil during steam reforming, Fuel 265 (2020), 116961, https://doi.org/10.1016/j.fuel.2019.116961.
[44] B. Valle, B. Aramburu, M. Olazar, J. Bilbao, A.G. Gayubo, Steam reforming of raw bio-oil over Ni/La_2O_3-αAl_2O_3: influence of temperature on product yields and catalyst deactivation, Fuel 216 (2018) 463–474, https://doi.org/10.1016/j.fuel.2017.11.149.
[45] C. Wu, L. Dong, J. Huang, P.T. Williams, Optimising the sustainability of crude bio-oil via reforming to hydrogen and valuable by-product carbon nanotubes, RSC Adv. 3 (2013) 19239–19242, https://doi.org/10.1039/c3ra43828g.
[46] L. He, S. Hu, L. Jiang, G. Liao, L. Zhang, H. Han, X. Chen, Y. Wang, K. Xu, S. Su, J. Xiang, Co-production of hydrogen and carbon nanotubes from the decomposition/reforming of biomass-derived organics over Ni/α-Al_2O_3 catalyst: performance of different compounds, Fuel 210 (2017) 307–314, https://doi.org/10.1016/j.fuel.2017.08.080.
[47] A. Arandia, A. Remiro, L. Oar-Arteta, J. Bilbao, A.G. Gayubo, Reaction conditions effect and pathways in the oxidative steam reforming of raw bio-oil on a Rh/CeO_2-ZrO_2 catalyst in a fluidized bed reactor, Int. J. Hydrogen Energy 42 (2017) 29175–29185, https://doi.org/10.1016/j.ijhydene.2017.10.095.
[48] A. Remiro, A. Ochoa, A. Arandia, P. Castaño, J. Bilbao, A.G. Gayubo, On the dynamics and reversibility of the deactivation of a Rh/CeO_2-ZrO_2 catalyst in raw bio-oil steam reforming, Int. J. Hydrogen Energy 44 (2019) 2620–2632, https://doi.org/10.1016/j.ijhydene.2018.12.073.
[49] B. Valle, B. Aramburu, P.L. Benito, J. Bilbao, A.G. Gayubo, Biomass to hydrogen-rich gas via steam reforming of raw bio-oil over Ni/La_2O_3-αAl_2O_3 catalyst: effect of space-time and steam-to-carbon ratio, Fuel 216 (2018) 445–455, https://doi.org/10.1016/j.fuel.2017.11.151.
[50] M. Hasan, J. Drazin, S. Dey, R.H.R. Castro, Synthesis of stoichiometric nickel aluminate spinel nanoparticles, Am. Mineral. 100 (2015) 652–657, https://doi.org/10.2138/am-2015-4997.
[51] M. Nuñez Meireles, J.A. Alonso, M.T. Fernández Díaz, L.E. Cadús, F.N. Aguero, Ni particles generated in situ from spinel structures used in ethanol steam reforming reaction, Mater. Today Chem. 15 (2020) 1–15, https://doi.org/10.1016/j.mtchem.2019.100213.
[52] O. Shtyka, Z. Dimitrova, R. Ciesielski, A. Kedziora, G. Mitukiewicz, J. Leyko, W. Maniukewicz, A. Czylkowska, T. Maniecki, Steam reforming of ethanol for hydrogen production: influence of catalyst composition (Ni/Al_2O_3, Ni/Al_2O_3-CeO_2, Ni/Al_2O_3-ZnO) and process conditions, React. Kinet. Mech. Catal. 132 (2021) 907–919, https://doi.org/10.1007/s11144-021-01945-6.
[53] A. Remiro, B. Valle, A.T. Aguayo, J. Bilbao, A.G. Gayubo, Steam reforming of raw bio-oil in a fluidized bed reactor with prior separation of pyrolytic lignin, Energy Fuels 27 (2013) 7549–7559, https://doi.org/10.1021/ef401835s.
[54] W.H. Chen, M.R. Lin, J.J. Lu, Y. Chao, T.S. Leu, Thermodynamic analysis of hydrogen production from methane via autothermal reforming and partial oxidation followed by water gas shift reaction, Int. J. Hydrogen Energy 35 (2010) 11787–11797, https://doi.org/10.1016/j.ijhydene.2010.08.126.
[55] R. Carapellucci, L. Giordano, Steam, dry and autothermal methane reforming for hydrogen production: a thermodynamic equilibrium analysis, J. Power Sources 469 (2020), 228391, https://doi.org/10.1016/j.jpowsour.2020.228391.
[56] A. Bali, J. Blanchard, M. Chamoumi, N. Abatzoglou, Bio-oil steam reforming over a mining residue functionalized with Ni as catalyst: Ni-UGSO, Catalysts 8 (2018), https://doi.org/10.3390/catal8010001.
[57] L. Oar-Arteta, A.T. Aguayo, A. Remiro, A. Arandia, J. Bilbao, A.G. Gayubo, Kinetics of the steam reforming of dimethyl ether over $CuFe_2O_4/\gamma$-Al_2O_3, Chem. Eng. J. 306 (2016) 401–412, https://doi.org/10.1016/j.cej.2016.07.075.
[58] N. Gao, K. Chen, C. Quan, S. Wu, Nickel supported over MCM-41 coated ceramic membrane for steam reforming of real tar, Int. J. Hydrogen Energy 46 (2021) 20882–20892, https://doi.org/10.1016/j.ijhydene.2021.03.213.
[59] L. He, G. Liao, S. Hu, L. Jiang, H. Han, H. Li, Q. Ren, M.E. Mostafa, X. Hu, Y. Wang, S. Su, J. Xiang, Effect of temperature on multiple competitive processes for co-production of carbon nanotubes and hydrogen during catalytic reforming of toluene, Fuel 264 (2020), 116749, https://doi.org/10.1016/j.fuel.2019.116749.
[60] L. He, G. Liao, H. Li, Q. Ren, S. Hu, H. Han, J. Xu, L. Jiang, S. Su, Y. Wang, J. Xiang, Evolution characteristics of different types of coke deposition during catalytic removal of biomass tar, J. Energy Inst. 93 (2020) 2497–2504, https://doi.org/10.1016/j.joei.2020.08.009.
[61] A. Ochoa, B. Aramburu, M. Ibáñez, B. Valle, J. Bilbao, A.G. Gayubo, P. Castaño, Compositional insights and valorization pathways for carbonaceous material deposited during bio-oil thermal treatment, ChemSusChem 7 (2014) 2597–2608, https://doi.org/10.1002/cssc.201402276.
[62] A. Ochoa, I. Barbarias, M. Artetxe, A.G. Gayubo, M. Olazar, J. Bilbao, P. Castaño, Deactivation dynamics of a Ni supported catalyst during the steam reforming of volatiles from waste polyethylene pyrolysis, Appl. Catal. B Environ. 209 (2017) 554–565, https://doi.org/10.1016/j.apcatb.2017.02.015.
[63] B. Lesiak, L. Kövér, J. Tóth, J. Zemek, P. Jiricek, A. Kromka, N. Rangam, C sp^2/sp^3 hybridisations in carbon nanomaterials – XPS and (X)AES study, Appl. Surf. Sci. 452 (2018) 223–231, https://doi.org/10.1016/j.apsusc.2018.04.269.
[64] H. Estrade-Szwarckopf, XPS photoemission in carbonaceous materials: a "defect" peak beside the graphitic asymmetric peak, Carbon 42 (2004) 1713–1721, https://doi.org/10.1016/j.carbon.2004.03.005.
[65] K. Dave, K.H. Park, M. Dhayal, Two-step process for programmable removal of oxygen functionalities of graphene oxide: functional, structural and electrical characteristics, RSC Adv. 5 (2015) 95657–95665, https://doi.org/10.1039/c5ra18880f.
[66] Y. Hu, X. Li, L. Zhang, M. Zhou, G. Wang, Y. Zhang, C. Xi, S. Cao, Mesoporous alumina as a solid phase extraction adsorbent for the determination of abamectin and ivermectin in vegetables by liquid chromatography-tandem mass spectrometry, Anal. Methods 6 (2014) 4734–4741, https://doi.org/10.1039/c4ay00107a.
[67] C. Montero, A. Remiro, B. Valle, L. Oar-Arteta, J. Bilbao, A.G. Gayubo, Origin and nature of coke in ethanol steam reforming and its role in deactivation of Ni/La_2O_3-αAl_2O_3 Catalyst, Ind. Eng. Chem. Res. 58 (2019) 14736–14751, https://doi.org/10.1021/acs.iecr.9b02880.
[68] A.C. Ferrari, J. Robertson, Interpretation of Raman spectra of disordered and amorphous carbon, Phys. Rev. B 61 (2000) 14095–14107, https://doi.org/10.1103/PhysRevB.61.14095.
[69] B. Valle, P. Castaño, M. Olazar, J. Bilbao, A.G. Gayubo, Deactivating species in the transformation of crude bio-oil with methanol into hydrocarbons on a HZSM-5 catalyst, J. Catal. 285 (2012) 304–314, https://doi.org/10.1016/j.jcat.2011.10.004.